A Study of the Aligned-Grid Retarding Potential Analyzer for Electric Propulsion Applications

Wensheng Huang*, Drew M. Ahern, and John T. Yim

National Aeronautics and Space Administration Glenn Research Center, Cleveland, OH, 44135, USA

* Corresponding author, wensheng.huang@nasa.gov. ORCID: 0000-0002-4647-3685.

Abstract:

During the development of energy analyzers for NASA's Solar Electric Propulsion Plasma Diagnostics Package, detailed studies were performed to compare the benefits and drawbacks of different types of gridded potential analyzers. In particular, modeling and testing were performed on three types of retarding potential analyzer with aligned grids, and one type with unaligned grids. Additionally, a type of gridded energy analyzer was tested. Analyses of the model and test results showed that manufacturing an analyzer with aligned grids required greater precision and knowledge than other analyzers. A properly designed analyzer with aligned grids exhibited superior signal level, acceptance angle control, energy resolution, and compactness compared to an analyzer with unaligned grids. Additionally, the gridded energy analyzer was found to accept a broad range of incidence angles while having superior signal, energy resolution, and compactness compared to retarding potential analyzer with unaligned grid. This article describes the basic design principles deployed in the study, the associated modeling work, and the characterization tests that were performed. The article summarizes the benefits and drawbacks associated with each type of energy analyzer tested.

Declarations

Funding

This work is entirely funded by the National Aeronautics and Space Administration Space Technology Mission Directorate Solar Electric Propulsion project.

Conflicts of interest/Competing interests

There are no conflicts of interest/competing interests.

Data availability

Data sets generated during the current study are available from the corresponding author on reasonable request. Certain information on the design of the test units not published in this article may be subjected to export control.

Code availability

The code CEX2D (an electrostatic ion trajectory solver) may be available from NASA on reasonable request. Commercial equivalent code is available to the public.

Authors' contributions

Wensheng Huang designed the sensors, supported testing, reduced the data, and co-developed the theories. Drew Ahern led the testing and development of test equipment. John Yim performed modeling and co-developed the theories.

Acknowledgments

We acknowledge Robert E. Thomas for supporting a portion of testing. We acknowledge Hani Kamhawi and the Space Nuclear Propulsion project for the opportunity to test an unaligned-grid RPA during a cluster thruster test. We acknowledge George J. Williams, Clayton D. Kachele, Penni J. Dalton, and Tiffany M. Morgan for project management leadership. We acknowledge Justin S. Fada, John Heese, David T. Jacobson, Frank Gatti, and Timothy W. Schuler for technical leadership. And we acknowledge Andrew S. Fausnaugh, Richard A. Kelsch, John J. Mayer, Kathleen J. Sukel, and Tiffany S. Vanderwyst for fabricating hardware and operating the facility.

1. Introduction

NASA stood up the Solar Electric Propulsion (SEP) Plasma Diagnostics Package (PDP) sub-project to produce a diagnostics package to characterize the plasma plume of high-power Hall thrusters in flight. While the project was discontinued in June 2022, a large amount of diagnostics development was accomplished, including detailed studies of the different types of multi-grid retarding potential analyzer (RPA) and a type of single-grid analyzer known as the wide-angle potential analyzer (WAPA). This article describes the experimental and numerical studies that were performed to better understand how changes in RPA interior geometry drove differences in the behavior of the diagnostics. The results of this work pointed to key geometric constraints that should be accounted for when designing aligned-grid RPAs.

The SEP PDP was originally conceived to tackle known gaps in high-power Hall thruster development. In particular, properties of the plasma plume during in-space operation are known to differ from ground test results due to facility effects [1-6] and accurate predictions of those properties have historically been difficult due to a lack of validation data. The intended target of the PDP was the 12-kW Advanced Electric Propulsion System (AEPS) Hall thruster that nominally operated at a discharge voltage of 600 V. The AEPS thruster is also intended to operate for more than twice as long as any previously flight-qualified thruster (up to 23,000 hours). Derived from these thruster characteristics, the corresponding plasma diagnostic sensors had to be capable of measuring an appropriate range of ion energies (up to 1000 eV was selected) and be able to withstand the plume-induced erosion over the service life of the thruster.

There are precedents in flying plasma diagnostics packages with new Hall thrusters. In 2000, Express III and A3 communication satellites were launched with Fakel SPT-100 Hall thrusters and plasma diagnostics located throughout the spacecraft [7]. In 2003, SMART-1 was launched with a Snecma PPS-1350 Hall thruster and plasma diagnostics at various locations around the spacecraft [8]. In 2006, TacSat-2 was launched with a Busek BHT-200 thruster and on-board plasma diagnostics [9]. In 2010, FalconSat-5 was launched with a Busek BHT-200 thruster and a high-speed plasma probe [10]. In 2012, AEHF-2 was launched with Aerojet Rocketdyne XR-5 thrusters and on-board plasma diagnostics [11]. In 2018, FalconSat-6 was launched with the same thruster and diagnostics systems as FalconSat-5 in order to gather additional data [12]. The proposed Asteroid Redirect Robotic Mission (ARRM) had planned to deploy a plasma diagnostics package to study the AEPS thruster [11]. More recent entries into flight plasma diagnostics for Hall thrusters include diagnostics packages on the Engineering Test Satellite 9 [13] and the Heinrich Hertz communication satellite [14]. The SEP PDP leveraged available information from these missions.

This article describes a novel approach to categorizing RPAs with aligned grids into three types based on the relative sizes of the bias and repel grid apertures. Testing and modeling work that were performed showed how differences in the macroscopic behavior of the three types of aligned-grid RPAs were driven by differences in the microscopic plasma mechanics. The article starts with a description of the design approach, RPA categorization, and performance metrics used to trade different designs. The article then describes the modeling and testing used to measure the performance of different RPA designs. Afterwards, this article describes similar work on the WAPA and offers a comparison of the advantages and disadvantages associated with the various potential analyzer designs.

2. Design Constraints and RPA Categorization

The SEP PDP sensors were designed for a reference plasma environment involving the operation of up to seven Hall thrusters, two of which are specifically targeted by PDP sensors. Given the plasma environment could involve the simultaneous operation of seven thrusters, a decision was made that certain PDP sensors must have small acceptance angles while others should have large acceptance angles. In particular, the RPAs were designed to have an acceptance angle wide enough to capture ions from a single 12-kW Hall thruster while rejecting ions from any other thrusters. In contrast, the WAPA had a large acceptance angle and was pointed at the plasma plume to capture only ions reflecting back towards the spacecraft due to plume interactions. These constraints were then combined with the expected locations of the sensors and predictions of the plasma environment from thruster ground tests to generate the expected plasma environment for each sensor type. Margins in the form 0.2x to 3x multipliers were added to account for facility-effect-related uncertainties. Table 1 summarizes the ranges of ion current density, ion energy, electron density, and electron temperature that the RPA and WAPA were designed for versus what they were tested to. From this table, one can see that the ion current density and electron density ranges over which the sensors must function were very wide, in large part driven by uncertainties about how the plume properties might change in-flight versus in ground tests. Due to limitations of the test setups, simulating the low end of the design ranges was not possible. In particular, the lowest densities that the test setup could simulate were approximately an order of magnitude higher than the lowest densities the WAPAs were expected to see in space.

Table 1. The design versus test plasma environments for the PDP RPA and WAPA.

Parameters	RPA design	RPA test	WAPA design	WAPA test
Ion current density, A/m^2	0.003 – 0.3	0.01, 0.2, 0.6	0.0005 – 0.035	0.01
Ion energy, eV	0 – 900	80 – 900	0 – 100	80 – 200
Electron density, m^{-3}	2.2e12 – 4.2e14	3e12 – 1.3e14	3.3e11 – 3.7e13	3e12 – 9e13
Electron temperature, eV	0.5 – 2	0.5 – 1	0.5 – 2	0.5 – 1

Given the constraints of small and well-defined acceptance angle plus the need to withstand long thruster firing duration without generating debris, the aligned four-grid design was selected for the RPA. An aligned-grid RPA is an RPA where the central axes of the apertures on each grid are aligned with each other, whereas in an unaligned-grid RPA the alignment of the aperture axes is random. Figure 1 shows a conceptual diagram of a four-grid RPA as well as the nomenclature for each electrode. From left to right in this figure, the electrodes are the floating grid, electron repel grid, bias grid, electron suppression grid, and collector. Each grid is a sheet with a regular pattern of perforations (referred to as apertures in this article) and the collector is a solid sheet. The floating grid is electrically floating and is meant to minimize perturbation of the local plasma outside the probe. The electron repel grid is biased negatively relative to ambient plasma potential to reject ambient electrons. The bias grid is biased positively to serve as a potential filter so that only ions with energy higher than the bias potential can pass through to the collector. Since secondary electrons ejecting from the collector distorts the result, the electron suppression grid is biased negatively relative to the collector to suppress said secondary electrons.

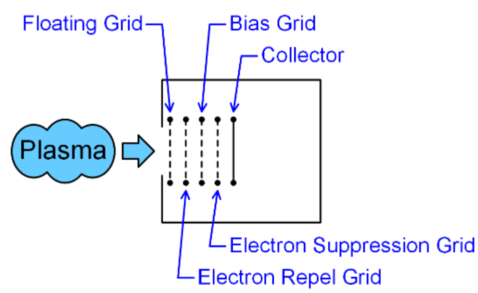

Figure 1. Conceptual diagram of a four-grid RPA showing nomenclature for each electrode.

During development, aligned-grid RPAs with a variety of geometries were modeled and tested. The team found that aligned-grid RPAs can be divided into three types based on the diameter of the aperture of the bias grid (also known as the ion retarding grid or ion discriminator grid) relative to the diameter of the aperture of the electron repel grid. For this article, type I is defined as when the bias grid aperture diameter is equal to the electron repel grid aperture diameter. Type II is defined as when the bias grid aperture diameter is less than the electron repel grid aperture diameter. Type III is defined as when the bias grid aperture diameter is greater than the electron repel grid aperture diameter. Table 2 summarizes these definitions. Bias grid aperture diameter is denoted by $Ø_{bias}$ while repel grid aperture diameter is denoted by $Ø_{repel}$. Also shown in Table 2 is the designation of the engineering development unit (EDU) design that corresponds to each RPA type.

Table 2. Types of aligned-grid RPA defined by relationship between bias and repel grid aperture diameters.

Type	Definition	Representative engineering unit
I	Aligned-grid RPA where $Ø_{bias} = Ø_{repel}$	EDU-V1
II	Aligned-grid RPA where $Ø_{bias} < Ø_{repel}$	EDU-V2
III	Aligned-grid RPA where $Ø_{bias} > Ø_{repel}$	EDU-V3

For measuring ions that are reflected back towards the spacecraft due to plume interactions, the one-grid WAPA design was selected for simplicity and wide acceptance angle. Figure 2 shows a conceptual diagram of the WAPA and the nomenclature associated with the electrodes. The screen grid is biased negatively relative to ambient plasma potential and the anode to both reject ambient electrons and suppress secondary electrons from the anode. The anode is biased positively to serve as a potential filter so that only ions with energy higher than the bias potential can reach the anode, and the anode current is measured.

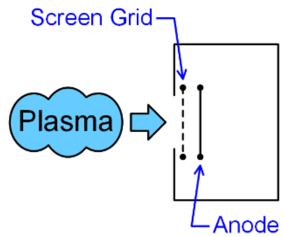

Figure 2. Conceptual diagram of the WAPA showing nomenclature for each electrode.

3. Modeling Approach

To assist in the design of the aligned-grid RPAs, electrostatic ion trajectory modeling was undertaken. An RPA with aligned grid apertures is essentially a gridded ion engine operating in reverse. The sensor slows down energetic ions to the point of repelling the ones below the bias potential. Thus, the CEX2D model, which has been successfully applied to gridded ion engine optics simulations [16], was modified to simulate the ion trajectories in RPAs.

CEX2D is a two-dimensional axisymmetric model of a single series of apertures [16]. Here, the "flux tube" ion beam portion of the model was used while aspects of the model related to neutral atoms, charge exchange collisions, and sputter erosion were neglected. Instead of accelerating ions from a source reservoir (i.e., the discharge chamber for ion engines), the model modified for RPA simulation assumed an inflow of monoenergetic ions that were accelerated or decelerated by the grid potential. The ions were modeled to enter the grid stack while perfectly collimated along the grid aperture axis, and the apertures were assumed to be perfectly aligned. The repel, bias, and suppression grids were modeled with perfectly straight bores and sharp corners while the floating grid was not modeled. This model was used to study how macroscopic behavior varied with geometric parameters. Metrics of interest included reduction in the electric potential in the bias aperture, number of ions impinging various grids, and measured energy distribution compared to actual energy distribution.

For certain evaluations of the design trade space, the Dakota package was utilized to enable the use of design-of-experiments principles in the computational assessments [17]. In particular, an orthogonal-array with Latin hypercube sampling approach was used to evaluate the main effects with a space-filling approach to explore potential new RPA grid designs.

3.1. Parametric Modeling of Bias Voltage Reduction at Center of Aperture

A parametric study was performed on the ratio of bias potential at the center of the aperture to the applied voltage, abbreviated as bias ratio, as functions of various geometric parameters. An ideal RPA will exhibit a bias ratio of unity, which implies no reduction in bias potential at center of the bias grid aperture. This parametric study revealed that the bias ratio was strongly affected by three parameters: the bias grid aperture diameter, the gap distance between the bias grid and both of its neighboring grids (repel grid and suppression grid), and the bias grid thickness. Note that the distances between the bias grid and each of its neighboring grids were set to be identical in this parametric study. The results are shown in Figure 3, Figure 4, and Figure 5. In these figures, the label "x μm gap" refers to the gap distance and the label "y μm thick" refers to the thickness of the bias grid. From these figures, one can see that the bias ratio moved closer towards unity with decreasing bias grid aperture diameter, increasing gap distance between grids, and increasing grid thickness.

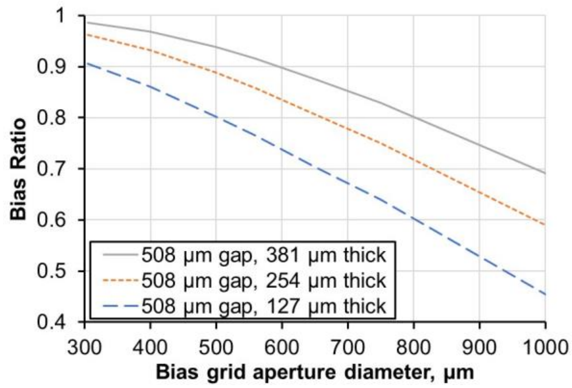

Figure 3. Bias ratio versus bias grid aperture diameter for 508 µm gap distance.

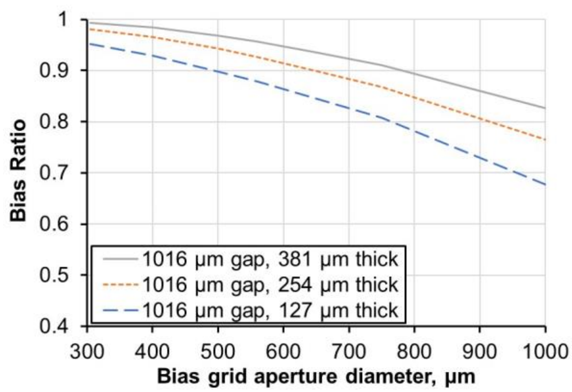

Figure 4. Bias ratio versus bias grid aperture diameter for 1016 µm gap distance.

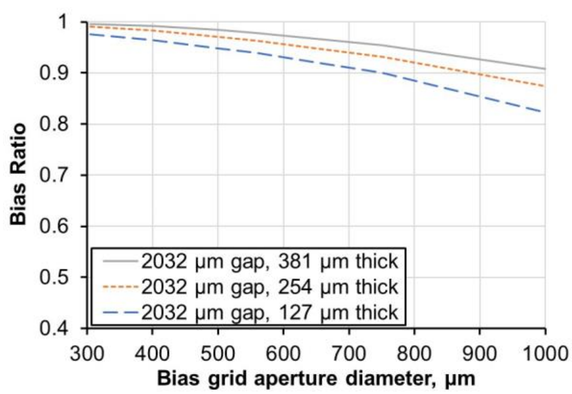

Figure 5. Bias ratio versus bias grid aperture diameter for 2032 µm gap distance.

4. Experimental Approach

To verify and validate simulation results, tests were performed on an engineering aligned-grid RPA of each type listed in Table 2, a laboratory unaligned-grid RPA, and several engineering WAPAs. The laboratory unaligned-grid RPA is also a four-grid RPA. The grids were confirmed in inspection to have no discernible alignment pattern. All grids of the unaligned-grid RPA were made from the same sheet metal with hexagonal aperture pattern, i.e., aperture diameter of all grids were the same. Note the unaligned-grid RPA was not modeled and was tested primarily to provide a comparison reference. Additional information on the design of and tests with this unaligned-grid RPA can be found in prior works [18-21].

Figure 6, Figure 7, and Figure 8 show images of the laboratory RPA, engineering RPA, and engineering WAPA, respectively. Each test article was tested in sensor characterization tests with an ion source and the tests were carried out with batches of up to four sensors at a time. Engineering sensors were also assembled into an engineering Thruster

Probe Assembly (TPA) for a wear test with an engineering model 12-kW Hall thruster. Figure 9 shows the TPA that went into the wear test.

Figure 6. Photo of a laboratory unaligned-grid RPA.

Figure 7. Photo of a representative engineering RPA.

Figure 8. Photo of a representative engineering WAPA.

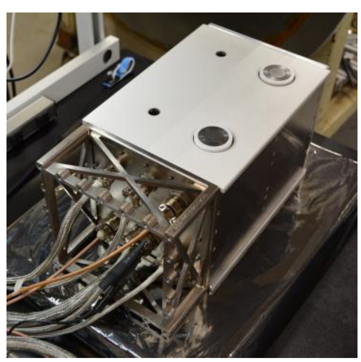

Figure 9. Photo of the TPA used for the wear test.

4.1. Test Setup

Figure 10 shows the test setup for the RPA sensor characterization test with major components labeled. The sensor characterization tests for the laboratory unaligned-grid RPA and the WAPA were similar except that different mounting brackets were used. The sensors being tested were mounted to the test plate, which was mounted to a rotary stage and a linear stage. The motion stages were configured such that the entrance of each sensor being tested could rotate in place to simulate ions entering the sensor at different angles. A laboratory guarded Langmuir probe was also mounted to the test plate for the purpose of checking that the ion source was functioning correctly for each test. This guarded Langmuir probe doubled as a Faraday probe when biased in ion saturation and was of a design that had a long history of use in electric propulsion testing [18, 19, 22, 23].

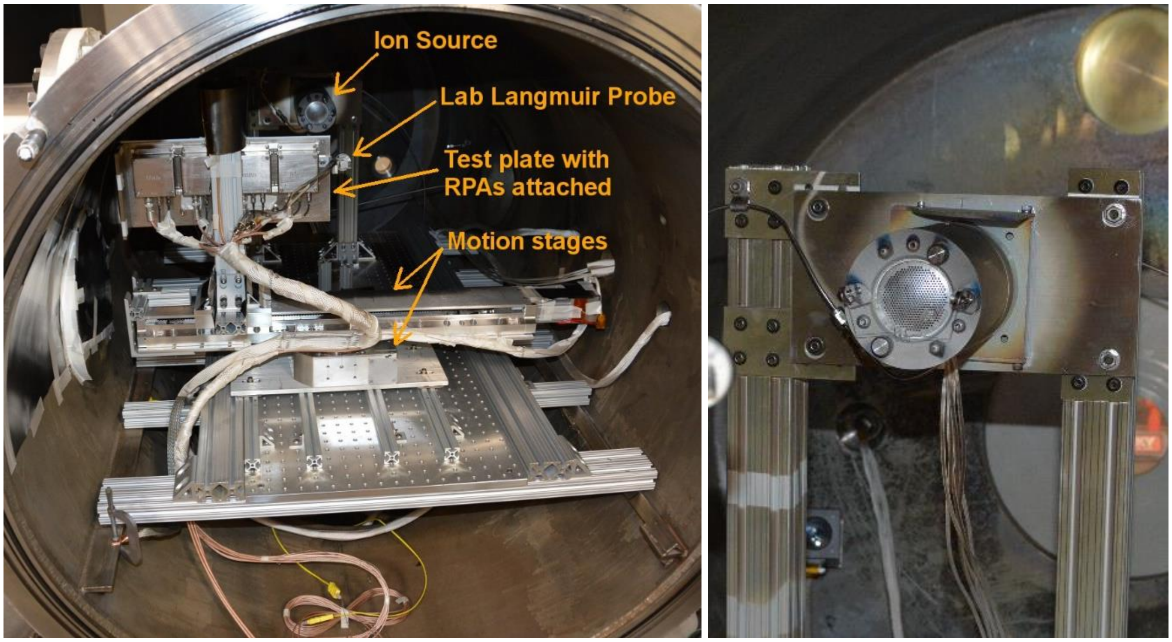

Figure 10. The RPA sensor characterization test setup (left) and the ion source (right).

The sensor characterization tests were carried out in Vacuum Facility 2 (VF2). The ion source was a Kaufman 40-mm gridded ion source operating on 6 sccm of research-grade xenon flow. Proper operation of the ion source was confirmed with a combination of electrical checks and guarded disk probe measurements prior to and periodically during the sensor characterization tests. The ion source was operated with vendor-supplied power electronics. The test articles were operated with commercially available power supplies and data acquisition devices. To ensure consistent test results, every sensor test began by exposing each test article to energetic plasma to remove surface oxides from the electrodes prior to performing the characterization test.

Note that because the PDP project was focused on characterizing aligned-grid RPAs, test of the laboratory unaligned-grid RPA as a function of ion incidence angle was not performed in VF2. Instead, data from an opportunistic test in VF6 involving the Hall-Effect Rocket with Magnetic Shielding (HERMeS) Technology Development Unit #1 and #3 (TDU1 and TDU3) [24] in a cluster configuration was used to estimate the acceptance angle of the unaligned-grid RPA. This cluster thruster test involved test points where one, the other, or both thrusters were operated. Figure 11 shows a diagram of the test setup for this cluster test. An unaligned-grid RPA of the same design used in the sensor characterization test was mounted to an arm that rotated around the TDU1 (labeled thruster A) while the TDU3 (labeled thruster B) was moved via a motion stage to achieve varying separation (labeled y_s) between the thrusters. The orange arc denotes the sweep path of the unaligned-grid RPA and a Faraday probe. In Figure 11, θ_A is the angle of the probe entrance position relative to the firing axis of thruster A where the reference position of the thruster is treated as the radial center of the thruster at its exit plane. Similarly, θ_B is the angle of the probe entrance position relative to the firing axis of thruster B. θ_I is the ion incidence angle at the probe entrance. From geometry, it can be shown that θ_I is equal to θ_B minus θ_A. During test points in which only TDU3 was operated while the unaligned-grid RPA was swept, the test configuration caused ions to enter the RPA at varying angles and plasma conditions. Assuming ions arrive from the reference position of TDU3, the known position of the probe can be used with the known position of TDU3 to calculate the ion incidence angle. By using the Faraday probe data collected at the same time as the RPA data, one can correct for the effect of varying input plasma conditions (albeit with increased measurement uncertainty compared to a dedicated angular response test) and obtain the equivalent of the probe's response versus angle so that the acceptance angle can be estimated. These corrections that are specific to the unaligned-grid RPA results will be described in the section on unaligned-grid RPA results. Additional details of the cluster test not relevant to this article will be published in future articles.

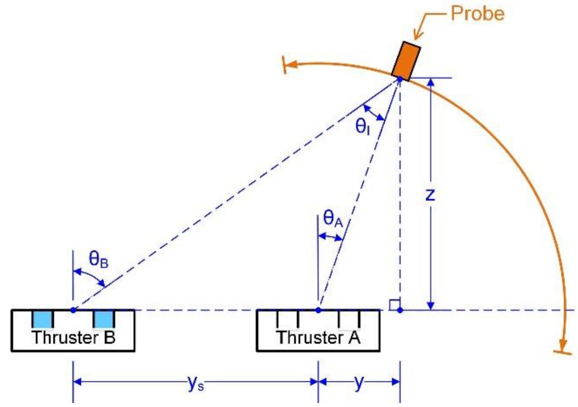

Figure 11. Cluster thruster test setup from which acceptance angle of the unaligned-grid RPA was assessed.

To assess behavior of the aligned-grid RPA and WAPA in a Hall thruster plasma environment, EDU-V1 RPAs and WAPAs were integrated into an engineering TPA and mounted in Vacuum Facility 5 (VF5) for a 645-hr wear test. In this test, the RPAs pointed at the AEPS engineering model thruster while the WAPAs pointed at the far-field. The thruster was operated at 600 V discharge voltage, and 11 and 12 kW discharge power when accumulating wear hours. The thruster was also operated at 300 V discharge voltage with 3-6.25 kW discharge power and 600 V, 9-12.5 kW periodically to provide reference data. The VF5 ground plasma diagnostics [25], which contained an unaligned-grid RPA of the same design used in sensor characterization test, were also used during this TPA wear test to provide additional reference data. More information about the thruster can be found in prior publications [26-28].

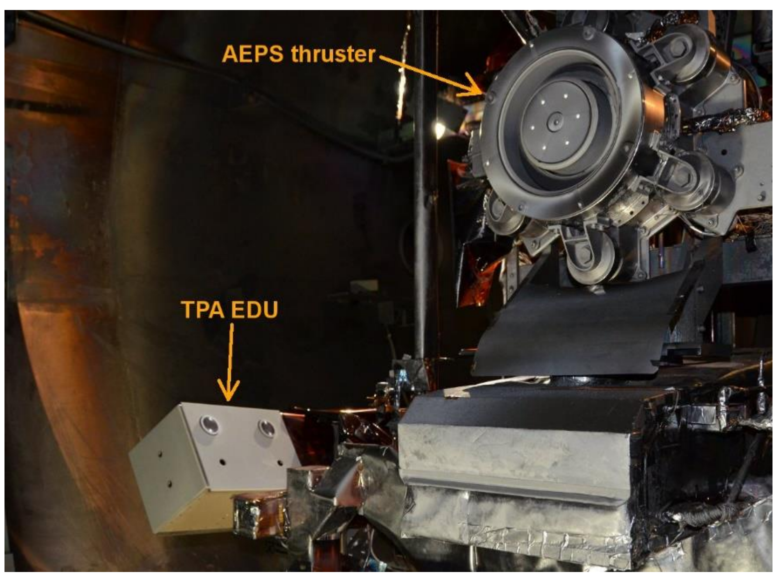

Figure 12. TPA EDU in a wear test with an AEPS engineering thruster.

During the TPA wear test, the TPA EDU was mounted such that the downstream-most surface was 80 degrees from the thruster firing axis. This was done to subject the assembly and sensors to a conservative amount of plasma from a wear perspective. For this wear test, the engineering sensors were operated with the same models of commercially available power supplies and data acquisition devices as in the sensor characterization tests. Only a portion of the wear test data pertinent to this article will be discussed. The rest of the wear test results were published elsewhere [15].

4.2. Data Reduction

Sensor data was analyzed using the same techniques developed for analyzing laboratory plasma diagnostics data for other AEPS thruster tests [25]. These techniques are briefly described below.

In all tests, a laboratory guarded disk probe was used to measure the local plasma potential near the analyzer being tested, and that plasma potential was subtracted from the power supply applied bias to get the actual bias experienced by the ions. This was done to account for the fact that the ion retarding grids of the analyzers were biased with respect to the facility ground while the incoming ions were at plasma potential.

Next, the RPA data was smoothed using a Savitzky-Golay filter [29, 30]. Then, the negative of the derivative of the collector current with respect to the ion retarding grid bias voltage was taken. The result, plotted against the bias voltage, was proportional to the ion energy per charge distribution function, which was the same as the ion energy distribution function (IEDF) for singly-charged ions [31]. The average ion energy per charge was calculated by averaging only the part of the trace where the amplitude exceeded half of the maximum amplitude. This averaging approach is referred to as the 50%-threshold-based averaging approach. Figure 13 shows an example of applying the 50%-threshold-based averaging approach to an RPA trace. The black dashed vertical line indicates the location of the most probable voltage, the red solid vertical line indicates the result of using the 50%-threshold-based averaging approach, and the red dashed horizontal line indicates the 50%-of-maximum threshold.

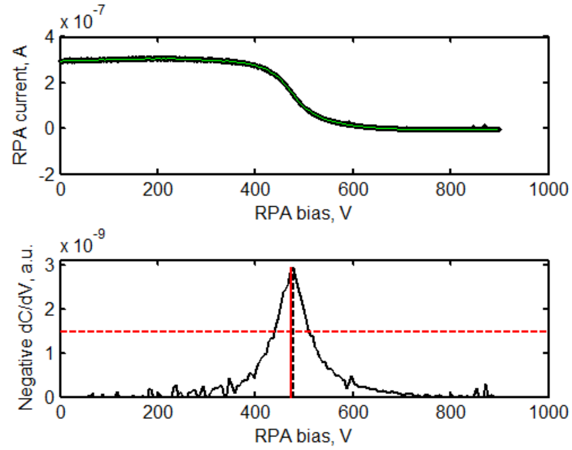

Figure 13. Example of RPA analysis.

In theory, the most accurate result would have been obtained by averaging the entire RPA trace (a.k.a. ensemble average). However, many RPA configurations generate low intensity tails that skew the ensemble average. This article will show later that the tails are artificial and likely due to ion impingement on various grids that can be difficult to avoid. Furthermore, without specific controls, RPAs are susceptible to accepting ions at large angles that will also show up as tails in the measurement. Another possible approach to analyzing the ion energy per charge distribution is to use the most probable energy. However, the most probable energy is determined by at most a few data points out of the entire distribution and is highly susceptible to measurement noise. Using the 50% threshold-based averaging approach largely avoids the effect of artificial tails driven by RPA geometries while being robust against measurement noise.

4.3. Performance Metrics

To systematically assess the behavior of various analyzer designs, definitions of certain key metrics are described here. The signal-to-noise ratio (SNR) is defined as the signal level divided by the root-mean-square of the noise at high enough bias to repel all incoming ions. Here, signal level is defined as the collector current at 0 V bias relative to the local plasma potential. These definitions are illustrated in Figure 14.

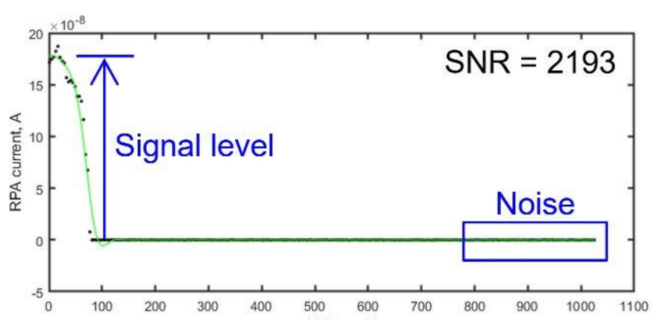

Figure 14. An example of how RPA signal-to-noise ratio is calculated.

Transparency is defined as the fraction of ions entering the entrance plane of the sensor that reaches the collector at 0 V bias. Transparency at 0° refers to the transparency when the velocity vector of the incoming ions is parallel to the normal vector of the entrance of the RPA (i.e., ion incidence angle of 0°). For a typical RPA, this value is also the maximum transparency. The ion current entering a potential analyzer is calculated from the ion current density measured by the guarded Langmuir probe multiplied by the known entrance area of the potential analyzer.

Two variants of acceptance angles are defined for this article. Acceptance angle, 50%, or δ_{50}, is defined as the ion incidence angle at which the signal level falls to 50% that of the maximum signal level. Acceptance angle, 10%, or δ_{10}, is defined as the ion incidence angle at which the signal level falls to 10% that of the maximum signal level. The former metric is useful for determining the cone within which the plasma is being properly measured by the sensor, while the latter metric is useful for determining the cone outside of which the plasma is being rejected by the sensor. Note that the flux density of the incoming ions is assumed to be constant while evaluating acceptance angle, and any deviation from this assumption must be corrected for.

Energy resolution is defined as the full-width-at-half-maximum energy of the ion energy per charge distribution derived from the RPA data assuming that the incoming ions are monoenergetic. This is a good assumption because the ion source used in testing has an energy width (defined as full-width-at-half-maximum) of less than 10 eV, according to the manufacturer, while all RPAs tested have energy resolutions much greater than 10 eV.

4.4. Measurement Uncertainties

Uncertainty in current measurements was limited by measurement electronics to ±0.3%. However, uncertainty in intensity (the y-axis of energy per charge distributions obtained from energy analyzers) was dominated by plasma-related noise when ions were able to pass through the ion retarding grid to strike the collector (seen in the noise magnitude being much greater on the left side of Figure 14 than the right side). By examining all characterization data collected, the uncertainty in intensity was determined to be less than ±3%. Uncertainty in transparency was driven by uncertainty in intensity and was ±3%. Uncertainty in energy measurements was limited by the resolution of the applied bias voltage and the need for plasma potential correction to ±2 eV. Similarly, uncertainty in energy resolution was ±2 eV. For the aligned-grid RPA and WAPA results, uncertainty in acceptance angle was limited by angular resolution of the tests to about ±1º and ±2.5º, respectively. For the unaligned-grid RPA, because acceptance angle data came from an opportunistic test, the uncertainty in acceptance angle was increased due to the non-optimized test setup to approximately ±6°.

5. Results

For all results from the ion source tests shown, the ions were assumed to be singly charged, and the energy of the incoming ions was calculated as the ion source beam voltage minus the plasma potential at the test article. This plasma potential was measured by the guarded Langmuir probe. Note that phrase "ion condition" is used in this article when describing the condition of the ions arriving at the entrance of the sensor being tested during ion source testing. This phrase will be in the form of "ion condition at aaa eV, bbb A/m^2" where "aaa" is the ion energy and "bbb" is the ion current density.

5.1. Unaligned-grid RPA Results

The unaligned-grid RPA, aligned-grid RPA, and the WAPA all feature the same diameter entrance bore. The unaligned-grid RPA uses four grids made from sheet metals perforated with hexagonal pattern of apertures. The diameter of the grid apertures in the unaligned-grid RPA was fixed and was approximately the same size as the smallest diameter aperture used in the aligned-grid RPA (see Figure 26 for a visualization of the range of aperture diameters used in the aligned-grid RPAs). Aside from making sure the grids were parallel to each other, no attempt was made to control the orientation of each grid relative to each other grid. Figure 15 shows the non-dimensionalized grid stack cross section of the unaligned-grid RPA. In this figure, grid A is the floating grid, B is the electron repelling grid, C is the bias grid, and D is the electron suppression grid. From discussions with the Air Force personnel who designed this RPA, the spacings between grids were determined from repeated experimentation. For example, the spacing between the bias grid and electron suppression grid is large due to experiments showing that smaller spacing led to unacceptable distortions in the results as judged by the designers. The total height of grid stack for the unaligned-grid RPA was approximately three times as tall as the grid stack for the aligned-grid RPAs. This height could likely be decreased but the process of doing so required repeated iterations between design and tests. The complexity of the plasma physics associated with unaligned-grid RPA was such that any modeling effort would be prohibitive expensive compared to iterating between design and test. The current lack of ability to model an unaligned-grid RPA versus the readiness with which an aligned-grid RPA can be modeled (see section on aligned-grid RPA early results) is a key feature that distinguishes these two types of RPAs.

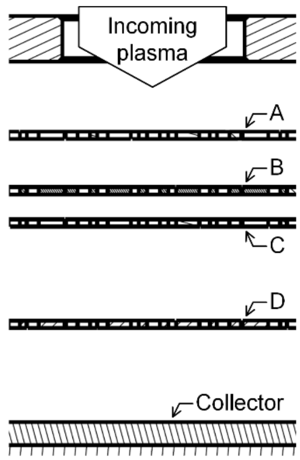

Figure 15. Grid stack cross section for the unaligned-grid RPA.

In the plasma response test of the laboratory unaligned-grid RPA, the ion incidence angle was set to 0° (ions parallel to normal axis of the entrance), the incoming plasma condition was varied, and the response of the sensor was assessed. This test characterized the transparency (when incoming ions were monoenergetic) and energy resolution associated with the sensor. Since the incoming ions were monoenergetic, the response of the sensor could also be studied for artificial distortions (e.g., two peaks when there should only be one, low intensity tails, negative intensity population). Figure 16 shows the reduced data from the unaligned-grid RPA with ion condition at 600 eV, 0.6 A/m^2. Red arrows were added to highlight the presence of negative (and unphysical) ion populations.

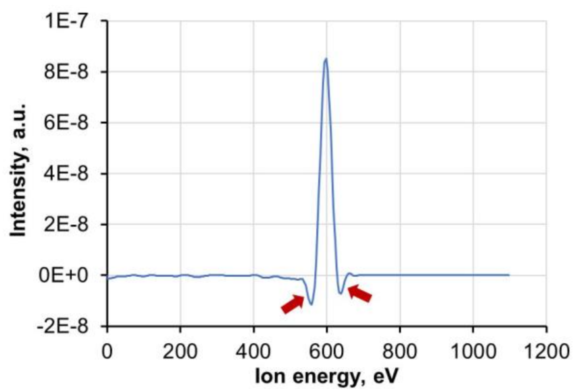

Figure 16. Reduced unaligned-grid RPA data with ion condition at 600 eV, 0.6 A/m^2.

To assess the accuracy of the unaligned-grid RPA for measuring the averaged ion energy, the difference between the ion energy and the RPA measurement using 50%-threshold-based averaging is plotted as a function of the ion energy in Figure 17. Similarly, the difference between the ion energy and the RPA measurement using ensemble averaging is plotted as a function of ion energy in Figure 18. Note that four sets of tests were performed to provide a variety of incoming ion energies and ion current densities. In particular, the "full power" set represented the maximum ion current density that could be provided by the ion source at a given ion energy and the ion current density varied from 0.028 to 1.5 A/m^2. For this ion source, the maximum ion current density increased monotonically with beam voltage due to space charge effect. For the data set labeled as having current densities of 0.2 and 0.6 A/m^2, the ion current density as measured by the guarded Langmuir probe was within 3% of the indicated value. For the data set labeled as having current density of 0.01 A/m^2, the ion current density was between -20% and +3% of the indicated value due to limitations in control resolution associated with the ion source discharge current. From Figure 17, one can see that when utilizing 50%-threshold-based averaging, the error in the unaligned-grid RPA measurement was within ~4 eV of the actual ion energy for the tested plasma conditions. However, if ensemble averaging was used then, as seen in Figure 18, the error rises to ~25 eV. The error associated with the use of ensemble averaging can be attributed to the artifact seen in Figure 16 having a complex, non-symmetrical relationship with ion energy and ion current density.

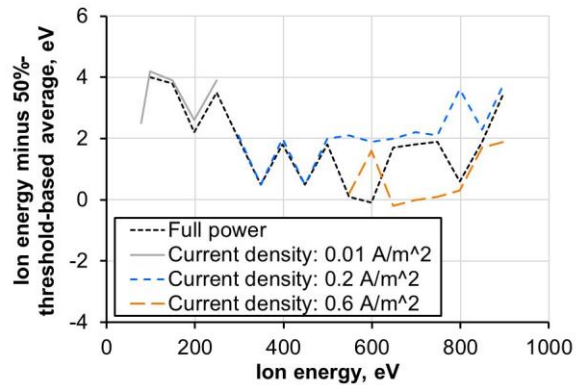

Figure 17. Ion energy minus 50%-threshold-based average for unaligned-grid RPA plasma response test.

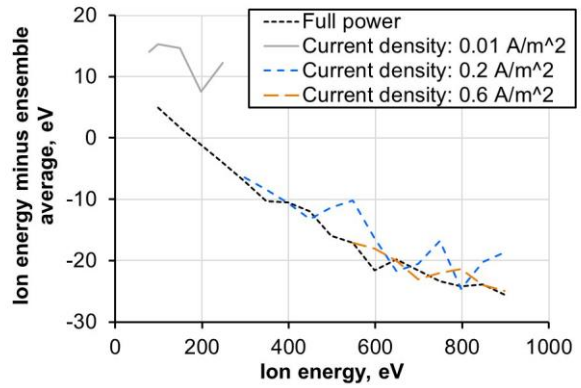

Figure 18. Ion energy minus ensemble average for unaligned-grid RPA plasma response test.

To facilitate comparison of the different energy analyzers studied in this article, the transparency and SNR of the unaligned RPA at 0° incidence in ion source testing were calculated. For the ion conditions tested (ion energy from ~80 to ~900 eV, ion current density from 0.01 to 1.5 A/m^2), transparency of the unaligned RPA varied from 0.01 to 0.03 and SNR varied from 122 to 12600. Figure 19 and Figure 20 show the transparency of the unaligned-grid RPA as functions of ion energy and ion current density, respectively, in ion source plasma. From these figures, one can see that transparency was largely independent of the ion energy and was fairly insensitive to ion current density except when ion current density dropped below ~0.1 A/m^2.

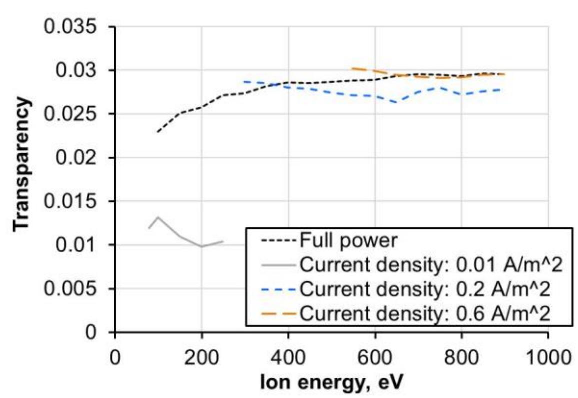

Figure 19. Transparency at 0° incidence versus ion energy for the unaligned-grid RPA in ion source plasma.

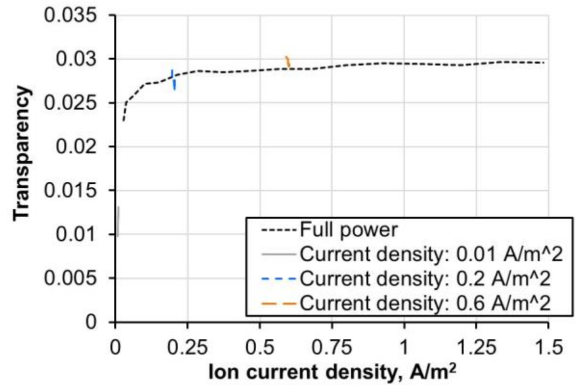

Figure 20. Transparency at 0° incidence versus ion current density for the unaligned-grid RPA in ion source plasma.

Figure 21 and Figure 22 show the SNR of the unaligned-grid RPA as functions of ion energy and ion current density, respectively. From these figures, the SNR was largely insensitive to both ion energy and ion current density except at low values of ion current density. This trend can be explained by a reduction in signal level as ion current density decreased. Additionally, there was a gradual reduction in SNR as the ion energy increased and this trend was driven by an increase in noise as the ion energy increased. One possible explanation was that as the ion energy increased, collision of these ions with various grids and insulators led to the release of an increasing number of secondary electrons. Although these electrons eventually recombined at various surfaces, during the brief time they existed these electrons created electromagnetic disturbances that propagated into the collector signal line. The greater the number of these transient secondary electrons that were created the greater the level of noise recorded on the collector.

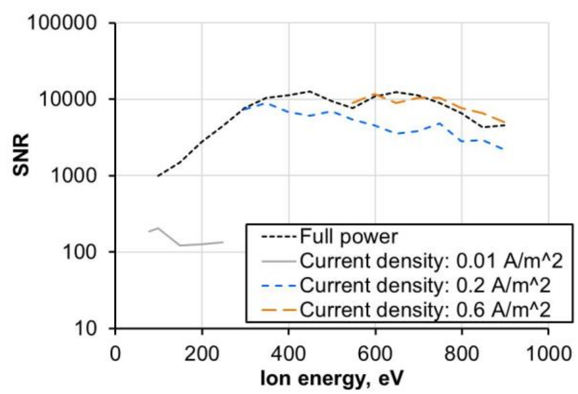

Figure 21. SNR versus ion energy for the unaligned-grid RPA in ion source plasma.

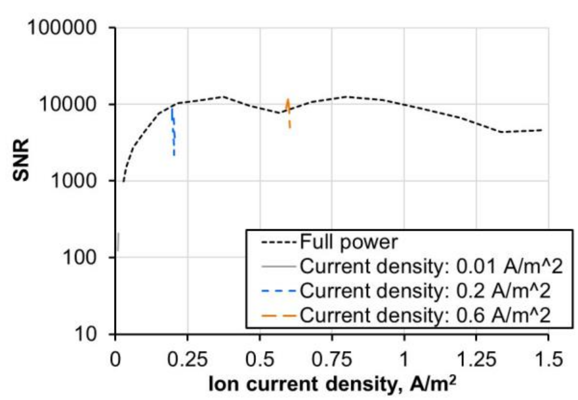

Figure 22. SNR versus ion current density for the unaligned-grid RPA in ion source plasma.

Additionally, the unaligned-grid RPA was swept through the plasma of TDU3 during the TPA wear test. From the resulting data, one can calculate the transparency of the probe in this Hall thruster plume, and this value ranged from 0.012 to 0.046. Figure 23 and Figure 24 show the transparency of the unaligned-grid RPA as functions of 50%-threshold-averaged ion energy as measured by the RPA and ion current density, respectively, in TDU3 plasma. Notably, there are two clusters of data points in Figure 23. In contrast, there are areas in Figure 24 where many values of ion current density corresponded to roughly the same value of transparency. The data appeared to imply a stronger correlation between transparency and ion energy than between transparency and ion current density. A possible explanation for this trend was that higher energy ions in the plume of a Hall thruster were beam ions originating from the discharge channel whereas lower energy ions were charge-exchange (CEX) products originating from a more diffused region in the near-field. As a result, the higher energy ions entered the RPA in a relatively collimated fashion while the lower energy ions entered from a range of incidence angles, and many of these lower energy ions were not able to pass through the grid stack to the collector. In contrast, the transparency was fairly constant down to relatively low ion energies in ion source tests, and this might be attributable to the fact that ions produced by the ion source were collimated even at low energy. A caveat to this observation on the ion source data was that at the lowest tested ion energy, which corresponds to the lowest tested ion current density of 0.01 A/m^2, there was an unexplained drop in transparency (see solid gray line in Figure 19 and Figure 20). This behavior was not likely to be due to CEX ions as the ion source was not known to produce a meaningful quantity of CEX ions when operating at low beam voltage and current density.

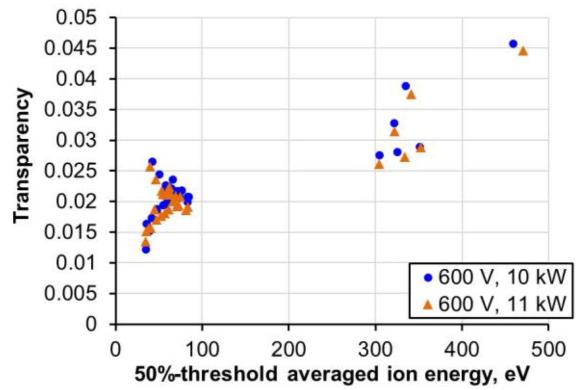

Figure 23. Transparency at 0° incidence versus measured ion energy for the unaligned-grid RPA in Hall thruster plasma.

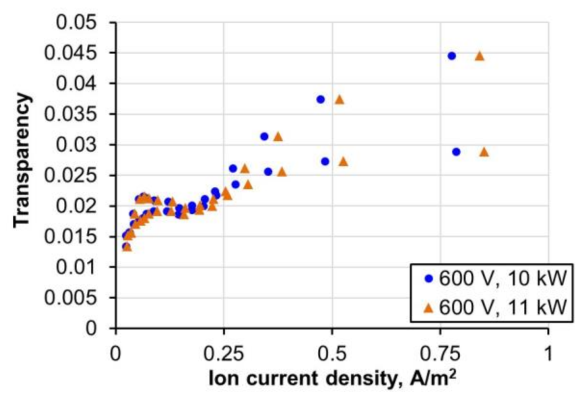

Figure 24. Transparency at 0° incidence versus ion current density for the unaligned-grid RPA in Hall thruster plasma.

Data for estimating the acceptance angle of the unaligned-grid RPA came from the opportunistic test described in the test setup section. Since the incoming current density varied with probe location, this effect was corrected for by defining a normalized current density, which is the current density at each probe location divided by the maximum current density in the corresponding data set. Then, the signal level was divided by the normalized current density. To facilitate plotting, the corrected signal level was normalized by the maximum value of the corrected signal level in the corresponding data set. Figure 25 shows the normalized signal level versus the ion incidence angle for all recorded data sets. In this figure, the voltage and power in the label refers to the discharge voltage and discharge power that the TDU3 was operating at, and the "config" number refers to the center-to-center separation between the thrusters. Config 1 corresponds to 604 mm separation and config 2 corresponds to 1000 mm separation. With the exception of the 300 V, 6 kW, config 1 data set, all data sets exhibited a general decrease in normalized signal level with increasing ion incidence angle. It was unclear why the 300 V, 6kW, config 1 data set exhibited a rise in normalized signal level near 15 degrees ion incidence angle, and this data set was excluded from acceptance angle calculations. By averaging the other three data sets and interpolating for when the average crossed the 50% threshold, δ_{50} was estimated to be 17 ± 6° (vertical magenta dotted line). Then, a curve-fit was performed to data at ion incidence angle of >5°, to avoid the apparent plateau in signal at <5°, and extrapolated to the 10% threshold to yield an estimate for the δ_{10} of 30 ± 10° (vertical green dotted line). Note the uncertainty was proportionally higher for δ_{10} when compared to δ_{50} due to the use extrapolation.

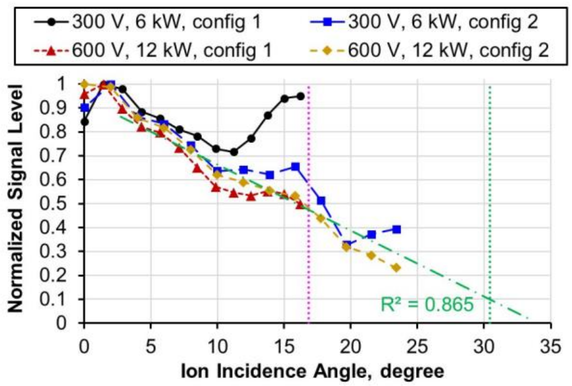

Figure 25. Normalized signal level versus incidence angle.

5.2. Aligned-grid RPA Early Results

Figure 26 shows the grid stack cross section of each of the aligned-grid RPA designs. Magenta lines were added to highlight the edges of one set of apertures for each design. In this figure, label A corresponds to the floating grid, B corresponds to the electron repel grid, C corresponds to the bias grid, and D corresponds to the electron suppression grid. Note the electron repel and electron suppression grids are electrically tied together.

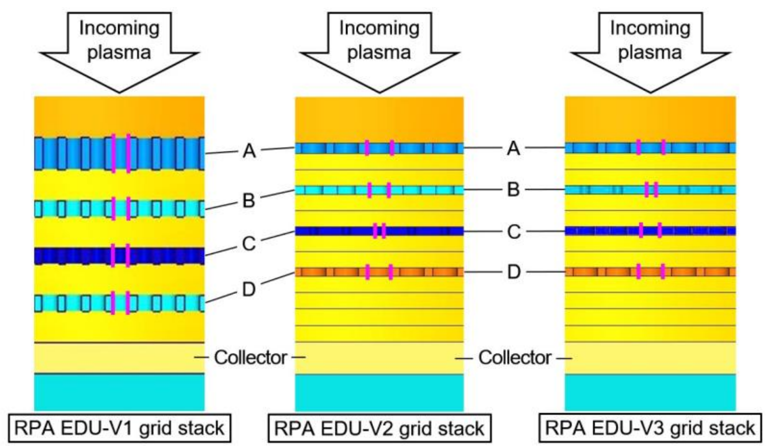

Figure 26. Comparison of the grid stack cross section for the three aligned-grid RPA designs tested.

At the start of each RPA sensor characterization test, each sensor unit was tested for electron backstreaming. In the electron backstream test, the electron suppression and repel voltage was swept over a range to determine the backstream limit. The backstream limit was defined as the electron suppression and repel voltage at which the bias grid current started to increase rapidly. In all RPA electron backstream tests, the backstream limit was found to be no lower than -8 V with respect to facility ground. During actual operation, the electron suppression and repel voltage was set to -35 V with respect to facility ground.

For an ideal RPA measuring monoenergetic plasma, like the ion source plasma, the collector current is constant as the bias voltage increases until the bias voltage reaches the ion energy, at which point the collector current rapidly decreases to zero as the bias voltage increases further. In short, an ideal RPA trace looks like a step function with the step occurring at the ion energy.

During initial testing with the RPA EDU-V1 (type I) with the ion source, the team discovered that the RPA traces exhibited anomalous behavior when compared to the ideal RPA trace. The collector current started decreasing at bias voltages about half as high as the ion energy. As the bias voltage neared the ion energy, the collector current increased again and then rapidly decreased to zero. When traces of RPA EDU-V1 were analyzed, it produced artificial low energy peaks that did not actually exist. Figure 27 shows raw traces from the RPA EDU-V1 and the laboratory RPA with ion condition at 600 eV, 0.2 A/m^2. The laboratory RPA trace was shown as a stand-in for what a more idealized trace would look like. Figure 28 shows the reduced RPA EDU-V1 trace. The presence of an artificial peak is highlighted in Figure 28. Note that four units of RPA EDU-V1 were tested in the same test session and all exhibited the same anomalous behavior.

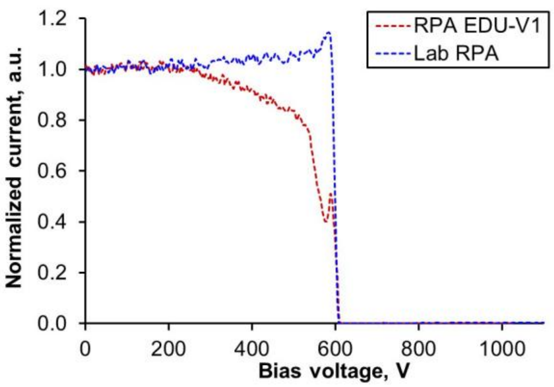

Figure 27. Raw data from RPA EDU-V1 and laboratory RPA with ion condition at 600 eV, 0.2 A/m^2.

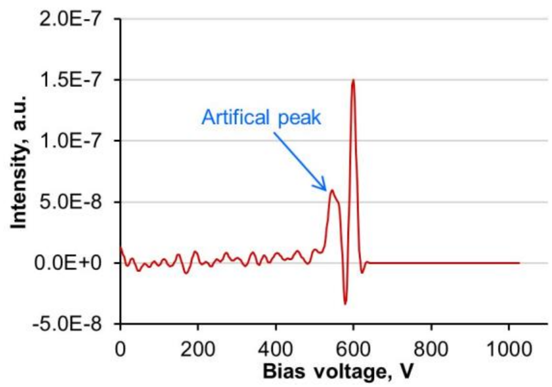

Figure 28. Ion energy distribution derived from RPA EDU-V1 data with ion condition at 600 eV, 0.2 A/m^2.

Numerical investigation using the model described in the ion physics modeling section suggested that incoming ions were experiencing varying degrees of impingement on the secondary electron suppression grid of the EDU-V1. This is illustrated in the left part of Figure 29 where select ion trajectories are shown as white lines, and the background is ion density. In this simulation, the incoming ions were mono-energetic at 600 eV. The simulation showed that as the ion retarding potential rose toward the ion energy, the axial velocities of the ions became smaller and smaller. Since the retarding electric field was not perfectly axial, ions gained varying amounts of radial velocities (depending on their exact location) that began to rival the axial velocities as the axial velocities decreased. When the bias grid potential was near but below the ion energy, the ions appeared to focus as they approached the bias grid aperture and then de-focus as they passed through. If the bias grid had negligible thickness, the ions passing through the bias grid aperture would increasingly impinge upon the secondary electron suppression grid due to the aforementioned de-focusing effect (see simulation case labeled “bias voltage: 580 V” in Figure 29). The EDU-V1 grid had a finite thickness, driven by wear-related requirement. Ions passing through the EDU-V1 bias aperture became increasing de-focused as the bias voltage increased, but at a bias voltage just below the ion energy, ions on the edge of the beam column underwent a double reflection, once on each side of the aperture, and directed through the electron repel grid aperture (see simulation case labeled “bias voltage: 595 V” in Figure 29). Further increase in bias voltage caused ions to be repelled by the bias grid and the collector current dropped rapidly to zero (see simulation case labeled “bias voltage: 605 V” in Figure 29).

The right part of Figure 29 shows the expected currents on the electron repel grid, bias grid, electron suppression grid, and collector corresponding to the ion trajectory simulation shown in the left part of the same figure. Text below the right part of Figure 29 describes which of the abovementioned phenomena dominated over which part of the bias voltage sweep. In addition to the false peak, impingement on the suppression grid led to an artificial broadening of the energy distribution at lower energies. Note the high degree of similarity between the simulated collector current in Figure 29 and the measured collector current in Figure 27.

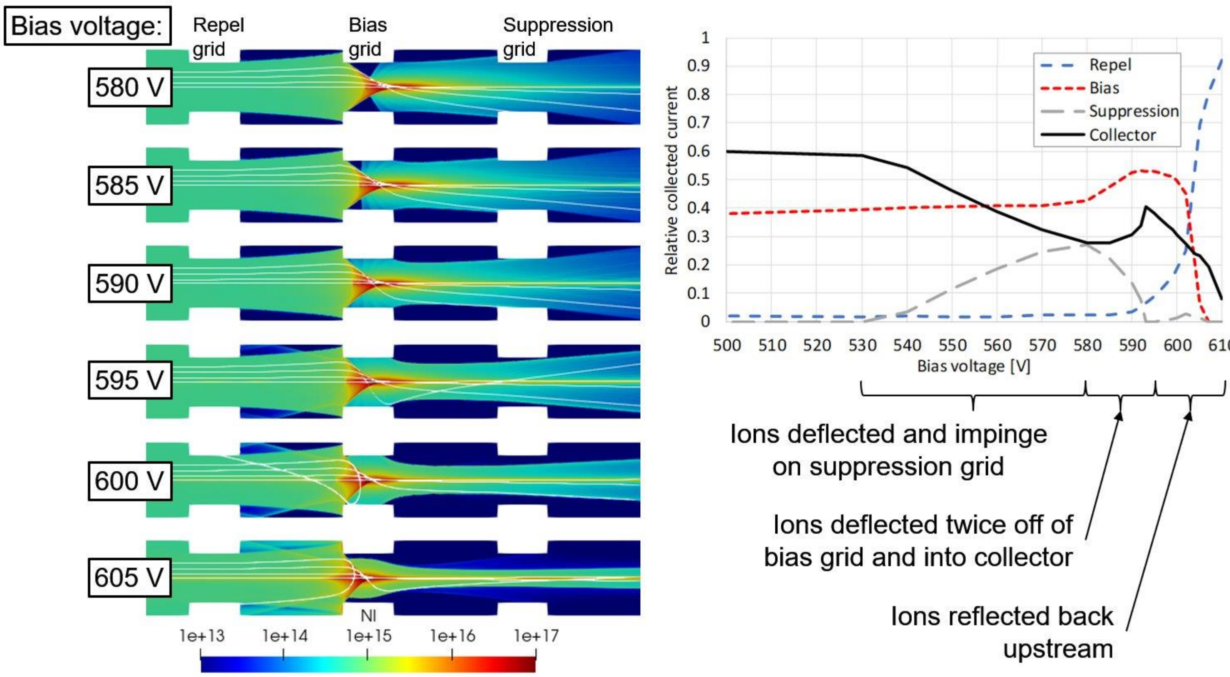

Figure 29. Simulations of ion trajectories (left) and grid currents (right) for the RPA EDU-V1 with incoming ions at 600 eV.

Data from the RPA EDU-V1 showed that the anomaly was very consistent across all tested ion conditions such that when both bias voltage and collector currents were normalized the resulting traces overlaid on top of each other. Figure 30 show RPA EDU-V1 traces at several ion conditions. This trend suggested that the anomaly was driven by electric field geometry rather than absolute values of the electric field, and number densities had no effect, which fits with the explanation suggested by the simulation. Other checks were also performed including sweeping the bias voltage at different rates and sweeping the bias voltage in the reverse direction.

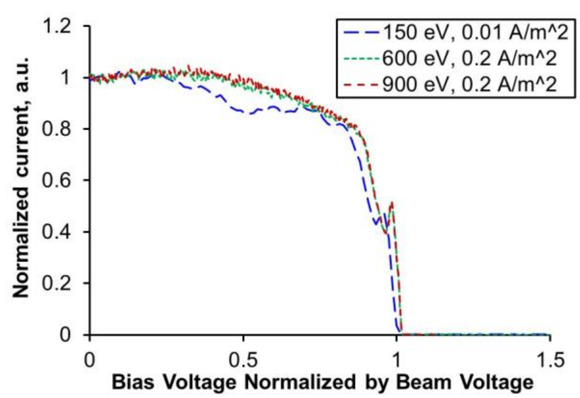

Figure 30. Normalized raw data from RPA EDU-V1 with various ion conditions.

With knowledge gained from EDU-V1, the team performed parametric studies while leveraging design-of-experiment principles as outlined in the ion physics modeling section to establish design parameters for the RPA that could produce measurements closer to the ideal trace. The space-filling design evaluations included manufacturing constraints on aperture length to diameter (L/D) ratios, grid thicknesses, and insulator thicknesses. In these studies, the team found that in order to minimize electron suppression grid impingement, the aperture of the electron suppression grid had to be much larger than that of the bias grid, and the bias grid to suppression grid gap had to be made as short as possible while maintaining electrical isolation and balancing any reduction in bias potential. Recall that per the parametric modeling results shown earlier, shortening the gap distance between the bias grid and suppression grid reduces the applied bias at the center of the bias grid aperture. The electron repel and suppression grids were found to generally maintain sufficient centerline potentials even at maximum applied bias grid voltages except for cases with low repel/suppression aperture L/D ratios. Furthermore, the gap distance between the repel grid and bias grid was found to have negligible impact for the design ranges examined. Repel grid to bias grid distance was set to be the same as the bias grid to suppression grid distance to simplify the design.

The trade space exploration found that two classes of RPA geometries, which are the type II and III previously listed, fitted the various constraints while producing RPA traces approaching the ideal. Since each grid included a large number of apertures and the overall RPA performance was dependent on the poorest performing apertures, uncertainty quantification incorporating known manufacturing tolerances was utilized to ensure the final designs were robust. These design activities resulted in two new RPA designs, which were designated EDU-V2 (type II) and EDU-V3 (type III). The thicknesses of the grids were also reduced when higher fidelity analysis decreased the uncertainty associated with the wear prediction. See Figure 26 for a comparison of the geometries across the RPA EDUs.

During sensor characterization test of the EDU-V2, another anomaly was discovered where the collected current suddenly increased at a bias voltage close to the ion energy before dropping to zero as the bias voltage increased. This result prompted detailed measurements of the grid currents as a function of bias voltage for all three aligned-grid RPA designs. Although simulations were never able to precisely replicate this specific collector current anomaly, the simulation and test data combined pointed to bias grid impingement as the most likely culprit. Figure 31 shows grid current measurements as functions of the bias voltage for the three aligned-grid RPA designs with the ion condition at 600 eV, 0.2 A/m^2. For this figure, "COL" refers to the collector, "BIA" refers to the bias grid, and "ESR" refers to the electron suppression and electron repel grids. Recall the electron suppression and electron repel grids are electrically tied together. In the middle sub-figure (corresponding to EDU-V2), one can see the aforementioned anomaly where the collector current slowly decreased but suddenly increased and then rapidly decreased as the bias voltage increased.

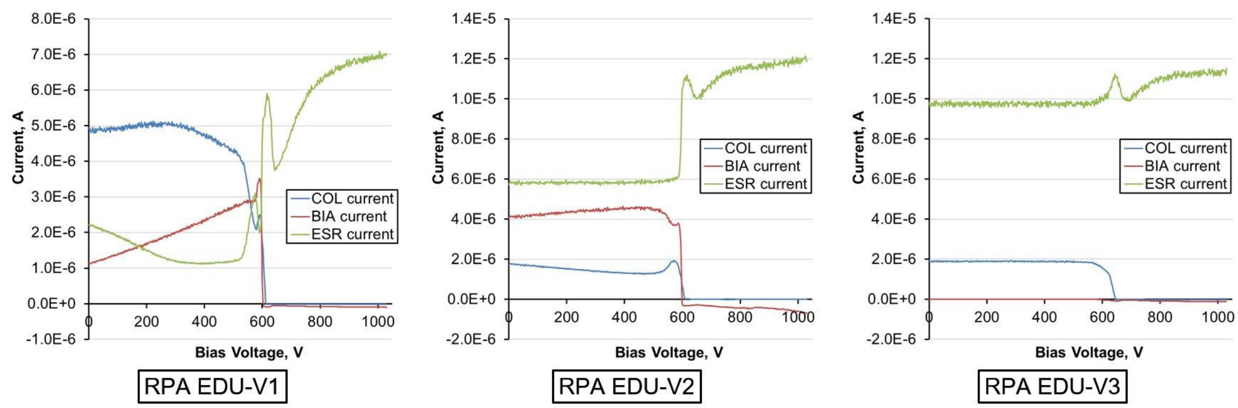

Figure 31. RPA grid current measurements for RPA EDU-V1 (left), EDU-V2 (middle), and EDU-V3 (right) with ion condition at 600 eV, 0.2 A/m^2.

Examination of Figure 31 left part (corresponding to EDU-V1) shows that, as predicted by simulation, there was a large amount of variation in the currents impinging on the EDU-V1 electron suppression and repel grids as bias voltage changed. This "ESR" current was fixed in both EDU-V2 and EDU-V3 up to the ion energy as the bias voltage increased from 0 V, which is illustrated by the horizontal green lines on the left portion of each sub-plot. Examination of Figure 31 middle part (corresponding to EDU-V2) shows that the variations in the collector current was synchronized with the variations in the bias grid current as the bias voltage increased. This trend strongly suggested that the EDU-V2 anomaly was related to bias grid impingement. Recall for EDU-V2, which is type II, the bias grid aperture was smaller than the electron repel grid aperture and the amount of ions impinging on the bias grid would ideally be constant. The current best hypothesis is that the focusing effect of the bias grid previously seen in EDU-V1 simulation caused a sudden increase in the number of ions that can pass through the bias grid aperture as the bias voltage increased. However, there was not a clear explanation for why the simulation was not able to predict the height of the anomalous peak in the collector current. Possible causes for the discrepancy included the inherent assumptions of the model such as axisymmetry, perfect geometries (no manufacturing defects), and collimated, aligned ion inflow.

Examination of Figure 31 right part (corresponding to EDU-V3) shows that the type III RPA design eliminated bias grid impingement as well as the anomaly observed in EDU-V2. Figure 32 shows RPA EDU-V3 modeling results. In the left part of this figure, select ion trajectories are shown as green, white, and magenta lines and the background is plasma potential. As with the EDU-V1, the model was able to accurately predict the behavior of the EDU-V3. The peak seen in the ESR current, which is the sum of electron suppression and electron repel grid currents, was found to primarily be a result of ions being repelled by the bias grid upstream into the electron repel grid. There were also trace amounts of electron suppression grid impingement. While further refinement is possible, the EDU-V3 design was satisfactory for the purposes of the PDP project.

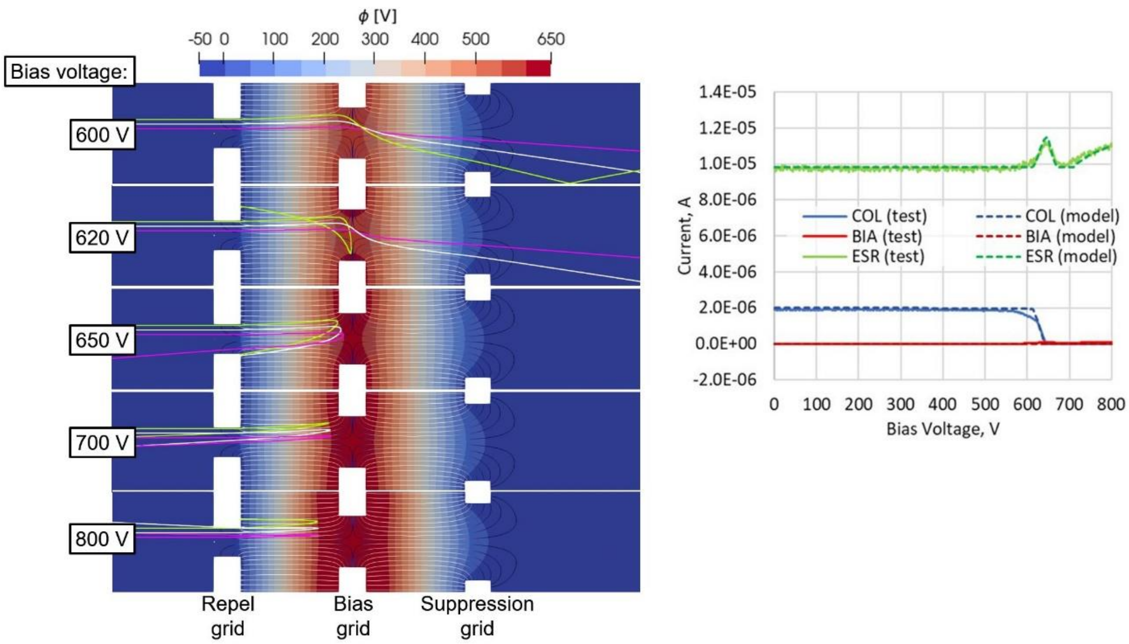

Figure 32. Simulations of ion trajectories (left) and grid currents (right) for the RPA EDU-V3 with incoming ions at 600 eV.

Although EDU-V3 provided a near ideal RPA trace, this design had a drawback. The bias grid aperture had to be made larger than the repel grid aperture and there was a physical limitation on how small the repel grid aperture could be. As a result, the bias grid aperture was of such a size that there was a measurable reduction in the retarding potential at the center of the aperture when compared with the applied voltage. In simulation and in tests, this reduction in bias potential scaled linearly with the bias voltage over a wide range of bias voltages. The team defined a new parameter called the bias voltage correction factor to account for this effect. The relationship between the actual bias voltage, the bias voltage correction factor, and the applied bias voltage is shown in Eq. 1.

$$\text{Actual Bias} = \text{Bias Voltage Correction Factor} * \text{Applied Bias} \qquad \text{Eq. 1}$$

In testing, the EDU-V3 bias voltage correction factor was found to be 0.947. The R-squared value of the linear fit was 1.0000. This correction factor value meant that bias power supply had to supply ~5% higher voltage to reflect ions of a given energy. The team determined that this trade-off for good RPA functionality in exchange for higher applied bias voltage was acceptable.

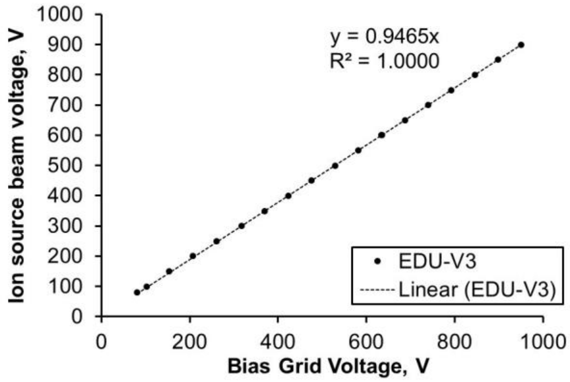

Figure 33. RPA EDU-V3 bias voltage calibration.

5.3. Aligned-grid RPA Final Results

For the aligned-grid RPA plasma response test, the list of ion source conditions tested was simplified to a single set. For this set, the 80 to 250 eV conditions were at 0.01 A/m^2, the 300 to 900 eV conditions were at 0.2 A/m^2, and a single condition at 600 eV, 0.6 A/m^2 was also tested. The reason only one condition from the 0.6 A/m^2 set was included was because differences between the laboratory RPA's response to 0.2 versus 0.6 A/m^2 conditions at any tested ion energy were trivial. The signal level scaled roughly with the ion current density, the IEDFs were the same, and all other characteristics were nearly identical. A single 0.6 A/m^2 condition was determined to be sufficient to catch any unexpected difference in the aligned-grid RPA that might be worth investigating. A total of five EDU-V1, one EDU-V2, and one EDU-V3 units were tested. The characteristics of the five EDU-V1 units were within measurement uncertainties of each other except for differences of up to 10% for the transparency measurements and related variations in SNR. The variations in transparency were likely due to manufacturing variations in the aperture diameter and grid-to-grid alignment as even a small variation on a small feature can greatly affect whether ions pass through or impinge on a grid. For the data shown in this article, representative data from EDU-V1 are shown except for transparency and SNR values. Ranges of EDU-V1 transparency and SNR shown are across all tested units while transparency and SNR at specific ion conditions are from a representative unit with behavior close to the middle of all tested EDU-V1 units.

Similar to the analysis of the unaligned-grid RPA data, the difference between the ion energy and the RPA measurement using 50%-threshold-based averaging is plotted as a function of the ion energy in Figure 34 for all three versions of RPA EDUs. This figure also includes the laboratory unaligned-grid RPA's response at the same ion source conditions for comparison. From Figure 34, one can see that the EDU-V2, EDU-V3, and laboratory RPA exhibited errors of ~5 eV max and were very similar to each other, but EDU-V1 exhibited errors of up to ~10 eV when measuring 400 eV ions and below and the error changed sign when ion energy went from 400 to 450 eV. Examination of the traces showed that the variation in the amplitude of the artificial peak was the main driver for this behavior. For ion conditions of ≤400 eV, the artificial peak was tall enough to exceed the 50%-of-maximum threshold and was included in the calculation for the average, thus pulling down the average. This same artificial peak was below the 50%-of-maximum threshold for ion conditions of ≥450 eV.

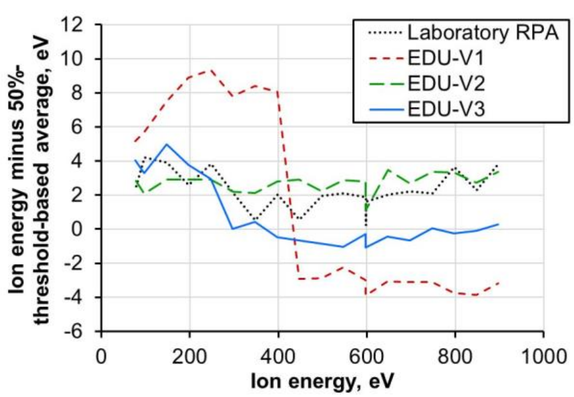

Figure 34. Ion energy minus 50%-threshold-based average for aligned-grid RPA plasma response test.

As with the unaligned-grid RPA, the response of the aligned-grid RPAs at 0° incidence were characterized. For the plasma conditions tested (ion energy from ~80 to ~900 eV, ion current density from 0.01 to 0.6 A/m^2), the transparency of the EDU-V1, EDU-V2, EDU-V3 varied from 0.124 to 0.252, 0.024 to 0.072, 0.052 to 0.078, respectively, and the SNR varied from 1800 to 78300, 638 to 13700, 743 to 17900, respectively. Figure 35 and Figure 36 show the transparency and SNR, respectively, of the aligned-grid RPA as functions of ion energy in ion source plasma. The values shown for EDU-V1 is from a representative unit whereas the ranges shown earlier are across all EDU-V1 units. As before, the values for the unaligned-grid RPA at the same ion source conditions are plotted for reference. From Figure 35, one can see that the aligned-grid RPAs have much better transparency than the unaligned-grid RPA, which can be attributed to the alignment of the grids promoting passage of ions through the grids. Furthermore, EDU-V1 has roughly three times the transparency as EDU-V3, which has slightly better transparency than EDU-V2. Higher transparency, particularly at low ion current density, leads to better SNR and better ability to detect sparse plasma like that found at high angles relative to the firing axis in a Hall thruster plume; see Figure 36, data points for 80 to 250 eV, which corresponded to the lowest tested ion current density of 0.01 A/m^2. Also, in Figure 36, it is notable that like the unaligned-grid RPA, the aligned-grid RPA exhibited a small decrease in SNR as the ion energy increased as seen in data corresponding to ion energy ≥300 eV, which corresponded to an ion current density of 0.2 A/m^2. The single outlier in this trend at 600 eV corresponds to ion current density of 0.6 A/m^2. The cause of the decrease in SNR at high ion energy for the aligned-grid RPAs is hypothesized to be the same as that for the unaligned-grid RPA.

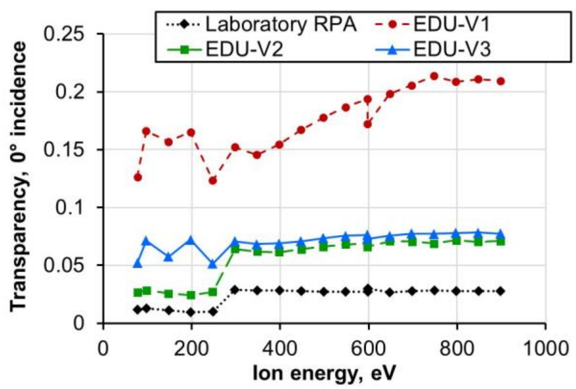

Figure 35. Transparency at 0° incidence versus ion energy for the aligned-grid RPAs in ion source plasma.

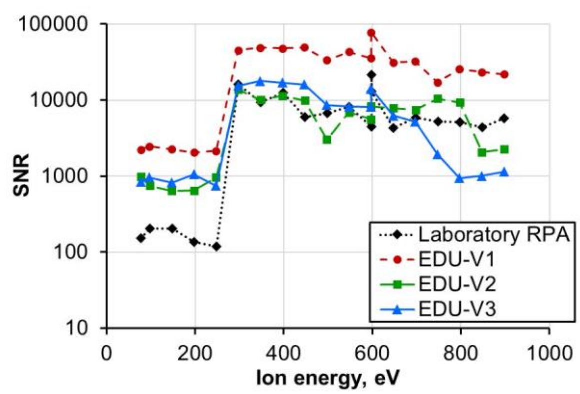

Figure 36. SNR versus ion energy for the aligned-grid RPAs in ion source plasma.

During the TPA wear test, two EDU-V1 units were mounted at fixed locations of 83° and 93° from the firing axis of the TDU3 Hall thruster. Data from both the unaligned-grid and aligned-grid RPAs showed that ions present at these locations were predominantly CEX ions. Over the tested thruster conditions, the EDU-V1 exhibited transparencies of 0.044 to 0.121. These transparency values were noticeably lower than those measured in ion source tests and the trend might be attributed to CEX ions coming into the sensor at a variety of incidence angles.

Angular response tests for the aligned-grid RPAs were carried out at five ion source conditions covering ion current densities of 0.01 and 0.2 A/m^2. Figure 37 shows the normalized signal level versus the incidence angle for a representative EDU-V1 unit. Note that in this and other similar figures for ion source angular response tests, the incidence angle can have positive or negative values because the rotary motion stage was turned in both directions to assess the symmetry of the RPA's response; by definition, the actual ion incidence angle is the absolute value of what is shown in these figures. From Figure 37, one can see that the EDU-V1 had nearly identical response across all tested ion source conditions. Calculated via interpolation and averaged across all ion source conditions, the acceptance angles δ_{50} and δ_{10} for EDU-V1 were 3.1 ± 1.0° and 5.6 ± 1.0°, respectively.

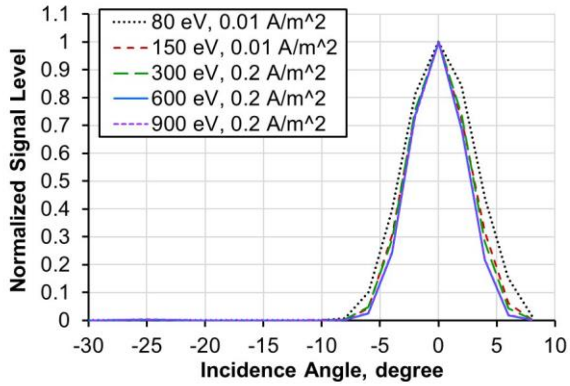

Figure 37. Normalized signal level versus incidence angle for a representative EDU-V1 RPA.

Notably, the anomalous behavior seen in EDU-V1 at 0° manifested differently at different incident angles. Figure 38 shows three examples of the EDU-V1 response for ion source condition of 600 eV, 0.2 A/m^2 covering incidence angles ranging from 2 to 8°. Figure 39 shows the corresponding IEDF after these data traces are reduced. From these figures, one can see that as the incidence angle increased, an ever sharper peak was observed at an energy just below the ion energy. These artificial structures showed up as both artificial positive and negative peaks in the corresponding IEDFs.

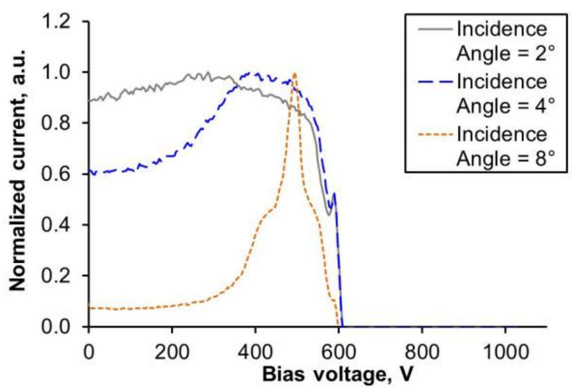

Figure 38. Data traces from EDU-V1 angular response test results.

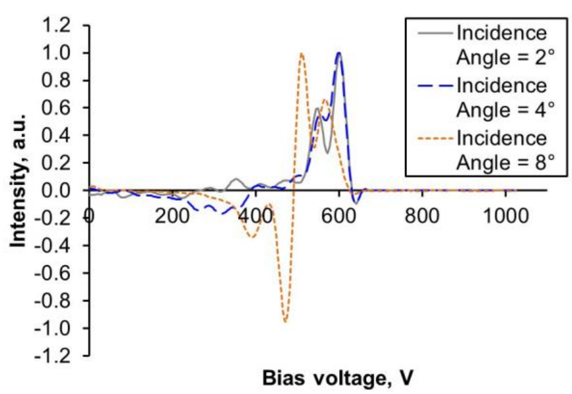

Figure 39. Reduced traces from EDU-V1 angular response test results.

Figure 40 shows the normalized signal level versus the ion incidence angle for the EDU-V2. The results at 150 eV for positive angles appeared out-of-family with other data sets, and there was not a clear explanation for this trend. However, exclusion of this out-of-family data would only change the averaged acceptance angle by 0.2°, which is much less than other sources of measurement uncertainty. Calculated via interpolation and averaged across all ion source conditions, the acceptance angles δ_{50} and δ_{10} for EDU-V2 were 4.9 ± 1.0° and 7.6 ± 1.0°, respectively. Figure 41 shows three examples of reduced data from EDU-V2 for ion source condition of 600 eV, 0.2 A/m^2 covering ion incidence angles ranging from 2 to 8°. Similar to EDU-V2 at 0° incidence, negative peaks and low energy tails were observed in these IEDFs.

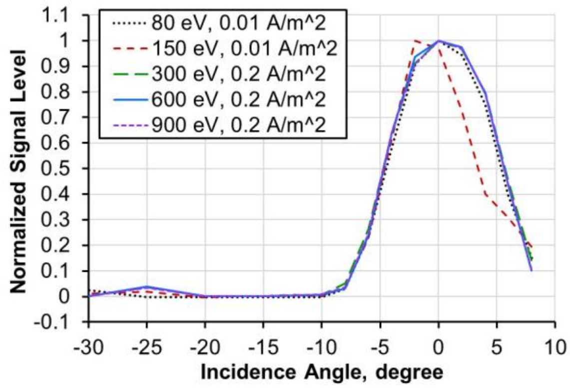

Figure 40. Normalized signal level versus incidence angle for EDU-V2.

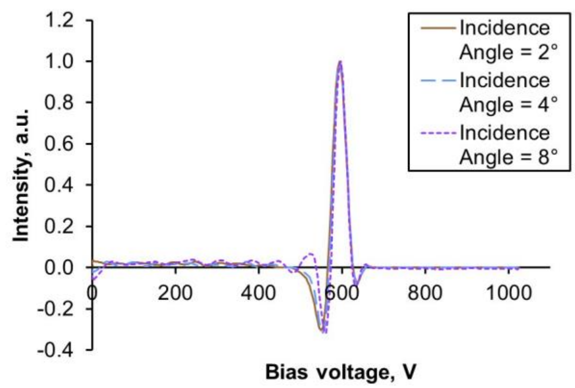

Figure 41. Reduced traces from EDU-V2 angular response test results.

Figure 42 shows the normalized signal level versus the ion incidence angle for the EDU-V3. Calculated via interpolation and averaged across all ion source conditions, the acceptance angles δ_{50} and δ_{10} for EDU-V3 were 7.3 ± 1.0° and 9.9 ± 1.0°, respectively. Figure 43 shows three examples of reduced data from EDU-V3 for ion source condition of 600 eV, 0.2 A/m^2 covering incidence angles ranging from 2 to 8°. Similar to EDU-V3 at 0° incidence, low energy bumps were observed in these IEDFs.

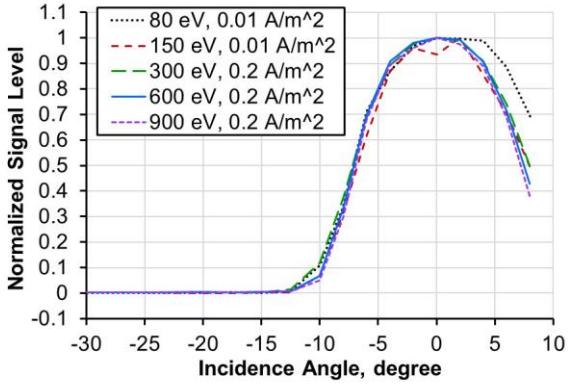

Figure 42. Normalized signal level versus incidence angle for EDU-V3.

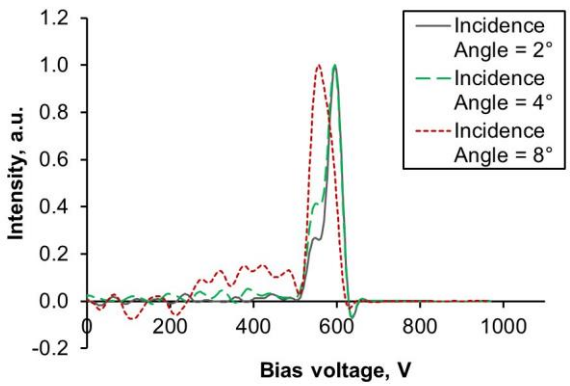

Figure 43. Reduced traces from EDU-V3 angular response test results.

Accuracy of the RPA measurement can also be assessed for the angular response tests, but the ion energy must be corrected for incidence angle because only the portion of the ion velocity parallel to the normal of the probe entrance will experience the retarding electric field inside the probe. The modified ion energy, E', as experienced by an RPA at an incidence angle of θ and in ions of energy E is given in Eq. 2, which is derived from geometry.

$$E' = E * (\cos\theta)^2 \qquad \text{Eq. 2}$$

Figure 44 shows the modified ion energy minus 50%-threshold-based average as a function of incidence angle for the EDU RPAs with ion source condition at 600 eV, 0.2 A/m^2. In this figure, only data at angles up to the plus and minus of δ_{10} of each EDU is shown because data beyond δ_{10} were nonsensical due to low SNR. From this figure, one can see that the anomalous behavior in EDU-V1 drove large errors in the resulting ion energy measurement, while EDU-V2 and EDU-V3 exhibited low errors within the angles where they responded most strongly to incoming plasma, i.e., within 5° to 6° or so. Both EDU-V2 and EDU-V3 exhibited increasingly large errors as the incidence angle increased.

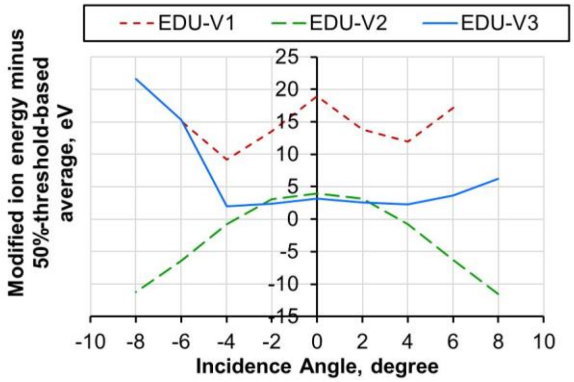

Figure 44. Error in measured ion energy as functions of incidence angle for the EDU RPAs with ion condition at 600 eV, 0.2 A/m^2.

5.4. WAPA Results

The WAPA had two operational modes, the normal mode and the screen mode. In the normal mode, the WAPA grid was biased to -35 V and the anode plate was swept to obtain an energy distribution (functionally the same as a gridded energy analyzer [31]). In the screen mode, the WAPA grid and anode were electrically tied and biased together, like a Langmuir probe. This article focuses on the operation of the WAPA in normal mode. WAPA normal mode tests were conducted in the same fashion as the RPA tests except that the WAPA was tested to a lower maximum ion energy and ion current density (see Table 1 for the differences in the tested environment). A total of four WAPAs were tested between the sensor characterization and TPA wear tests. Test results were identical between the tested WAPA units to within measurement uncertainty. For the data shown in this article, representative data from a WAPA will be shown except for transparency and SNR values. Ranges of WAPA transparency and SNR shown are across all tested units while transparency and SNR at specific ion conditions are from a representative unit with behavior close to the middle of all tested units.

As with the RPA, an electron backstream test was performed with the WAPAs. As the grid voltage was swept, the anode current was recorded. In all WAPA electron backstream tests, the backstream limit was found to be no lower than -6 V with respect to facility ground. Figure 45 shows the difference between the ion energy and the WAPA measurement using 50%-threshold-based averaging. The error was less than ~5 eV up to incident angle of 30°, beyond which the signal level dropped rapidly. For the plasma conditions tested (ion energy from ~80 to ~200 eV, ion current density of 0.01 A/m^2), the transparency of the WAPA varied from 0.201 to 0.240 and the SNR varied from 1400 to 2800. Note that while WAPA data was collected during the TPA wear test, because the plasma density was very low, the ion current density entering the WAPA could not be accurately measured and the associated transparency could not be calculated.

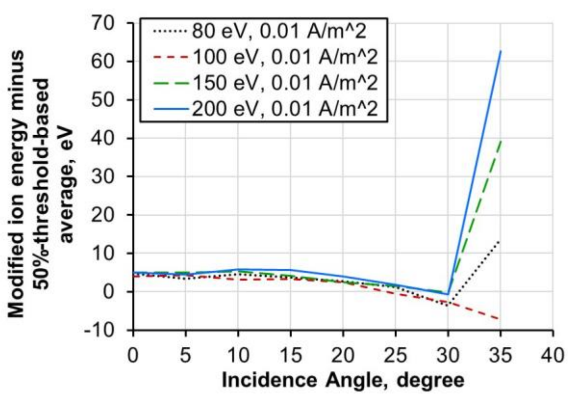

Figure 45. Error in measured ion energy as functions of incidence angle for a representative WAPA.

Angular response tests for the WAPAs were carried out at four ion source conditions. Only ion current density of 0.01 A/m^2 was tested because the WAPA was designed to operate at up to 250 V bias, and low ion energy corresponds to low ion current density for the ion source. Figure 46 shows the normalized signal level versus the incidence angle for a representative WAPA. From Figure 46, one can see that the WAPA had nearly identical response across all tested ion source conditions. Calculated via interpolation and averaged across all ion source conditions, the acceptance angles δ_{50} and δ_{10} for the WAPA were 15.3 ± 2.5° and 30.1 ± 2.5°, respectively. Note that based on line-of-sight calculation the theoretical maximum incidence angle for ions that can pass through the WAPA grid is ~40°, which is in good agreement with Figure 46 where the normalized signal level goes to ~0 at ~40°. Figure 47 shows four examples of reduced data from the WAPA for ion source condition of 150 eV, 0.01 A/m^2 covering incidence angles of 0 to 30°. No obvious artifacts were observed though the noise, seen as wriggles to the left of each peak, can mask low intensity artifacts. Figure 48 shows two traces at ion source condition of 200 eV, 0.01 A/m^2 from the same WAPA taken one day apart. Comparing these two traces, one can see that the oscillations to the left of the main peak were not repeatable and likely to be noise while the main peak was very repeatable. Also plotted were laboratory RPA data at the same ion source condition for reference. The laboratory RPA trace showed similar level of noise and the main peak was noticeably wider.

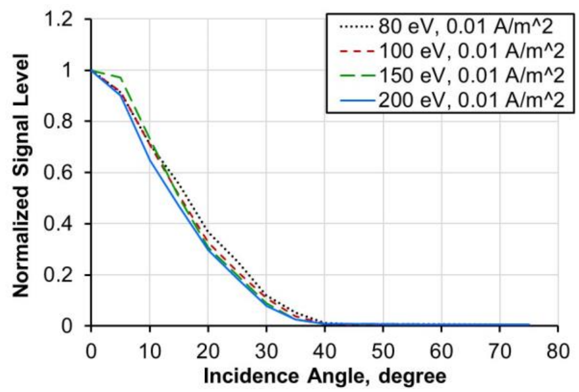

Figure 46. Normalized signal level versus incidence angle for a representative WAPA.

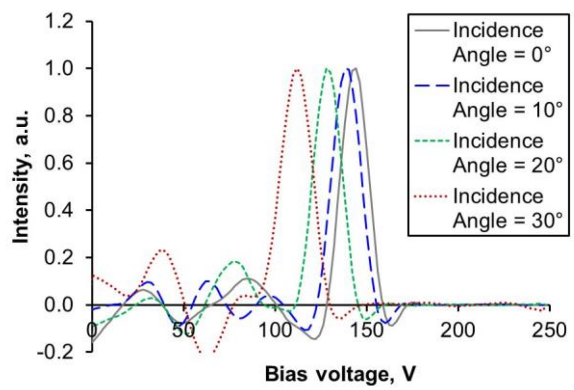

Figure 47. Reduced traces from WAPA angular response test results.

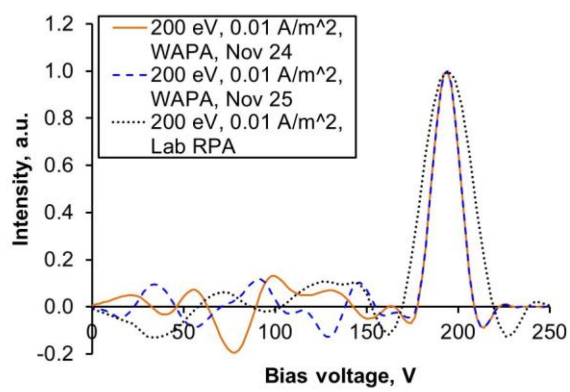

Figure 48. Reduced traces from WAPA and laboratory RPA with ion condition at 200 eV, 0.01 A/m^2.

5.5. Comparison of Potential Analyzers

Table 3 compares the performance metrics between the tested unaligned-grid laboratory RPA, aligned-grid engineering RPA, and WAPA. The laboratory RPA is designated as type U, which stands for an unaligned-grid RPA with the same aperture diameter on all grids. In Table 3, the third row gives a summary description of the IEDF anomalies present in each sensor design when at 0° incidence. In the same row, the anomalies present at non-zero incidence are described in parentheses, where "same" means the same type of anomalies as at 0° incidence were present. For the row on "transparency, 0°, ion source", the transparencies measured over all tested ion source conditions are listed as ranges, and then the transparency with ion condition of 600 eV and 0.2 A/m^2 is listed in parentheses. This parenthetical value provides a reference point representative of what a RPA may be subjected to when placed in the main beam of a Hall thruster operating at 600 V discharge, except that the ion source plasma is much more monoenergetic than Hall thruster plasma. Separately, transparency measured in Hall thruster plasma is also listed but this measurement was only taken for laboratory RPA and EDU-V1. Each of these two sensors were exposed to a range of conditions during the TPA wear test and the measured transparency are shown as ranges. To better compare laboratory RPA and EDU-V1, transparency at ~90° from the thruster firing axis for the thruster operating at 600 V, 11 kW are shown in parentheses. Note that the high ends of the ranges of SNRs are only directly comparable between the aligned-grid RPAs because all aligned-grid RPAs were tested to the same maximum ion current density of 0.6 A/m^2, while the unaligned-grid RPA was tested at up to 1.5 A/m^2 and the WAPA was tested at only 0.01 A/m^2. Energy resolution was assessed using data from ion source tests with ion condition at 600 eV, 0.2 A/m^2. For this energy resolution measurement to be accurate, the ion energy distribution of the ions produced by the ion source should be a few times narrower than the energy resolution of the RPA. From the manufacturer, the width of ion energy distribution of the ion beam from the ion source is no more than ~10 eV, which is sufficiently narrow. Stack height was defined as the distance from the top of the floating grid to the bottom of the collector plate.

Table 3. Comparison of performance metrics between various types of RPAs and the WAPA.

Parameter	Lab RPA	EDU-V1	EDU-V2	EDU-V3	WAPA
Type	U	I	II	III	
Presence of anomalies in IEDF at 0° incidence (anomalies at non-zero incidence)	Small negative peaks (not assessed)	Large artificial peaks (same plus negative peaks)	Small negative peak and long low-energy tail (same)	Small low-energy bump (same)	None detected (same)
Error in ion energy at 0° incidence, 50%-threshold-based average, eV	~4 max	~10 max	~4 max	~5 max	~5 max
Transparency, 0°, ion source (ion condition: 600 eV, 0.2 A/m^2)	0.010 – 0.030 (0.027)	0.124 – 0.252 (0.214)	0.024 – 0.072 (0.069)	0.052 – 0.078 (0.076)	0.201 – 0.240
Transparency, 0°, Hall thruster plume (thruster at 600 V, 11 kW; probe at ~90° from firing axis)	0.012 – 0.046 (0.019)	0.044 – 0.121 (0.052)	No measurement	No measurement	No measurement
SNR	122 – 12600	1800 – 78300	638 – 13700	743 – 17900	1400 – 2800
δ_{50} (Acceptance angle, 50%), degrees	17 ± 6	3.1 ± 1.0	4.9 ± 1.0	7.3 ± 1.0	15.3 ± 2.5
δ_{10} (Acceptance angle, 10%), degrees	30 ± 10	5.6 ± 1.0	7.6 ± 1.0	9.9 ± 1.0	30.1 ± 2.5
Energy resolution, at 600 eV, 0.2 A/m^2	30	18	24	22	No measurement
Energy resolution, at 150 eV, 0.01 A/m^2	29	29	16	20	17
Stack height, cm	2.03	0.76	0.72	0.72	0.23

From Table 3, one can see that a big advantage of the aligned-grid RPAs was that they had several times greater transparency than the unaligned-grid RPA, which led to correspondingly higher SNR values as seen in the low end of the ranges of SNR. The low end of the ranges of SNR shown are all measured at ion current density of 0.01 A/m^2. This result was not surprising since the uncontrolled grid alignment in the unaligned-grid RPA meant that the open area fraction through all four grids was low. All analyzers tested exhibited low errors except EDU-V1 due to its anomalous behavior. The WAPA exhibited no observable anomaly, the lab RPA and EDU-V3 exhibited minor anomalies, and EDU-V1 and V2 exhibited large anomalies.

The ability of the aligned-grid RPA to control acceptance angle compared to other analyzers is readily apparent in Table 3. When the target of interest is a specific thruster or a specific thruster region, only an analyzer with a small acceptance angle can reject plasma not from the target of interest. Conversely, in applications targeting the general plume, such as when measuring CEX products, the large acceptance angle associated with an unaligned-grid RPA or a WAPA is a better fit. A caveat is that, as seen in the derivation for modified ion energy (Eq. 2), ions arriving at a large incidence angle will be measured at a reduced energy by the sensor. Conversely, not knowing the incidence angle of the incoming ions complicates the analysis of an unaligned-grid RPA or WAPA. Furthermore, if the ions are monoenergetic but arrive with a range of incidence angles, the unaligned-grid RPA and WAPA will measure a broadened energy profile.

Generally, the energy resolution of the laboratory RPA and EDU-V1 were inferior to the other sensors, being larger by ~50%. This might be a consideration when measuring highly monoenergetic plasma plume like that of ion thrusters. In terms of compactness, the WAPA had the shortest grid stack, followed by the aligned-grid RPA. The unaligned-grid RPA had the tallest grid stack.

It is notable that the WAPA has similar or better performance than the laboratory unaligned-grid RPA across all metrics listed in Table 3. A caveat is that the PDP WAPA was built specifically for low bias voltages. Extending the present work to high bias voltages may be of value in demonstrating the utility of the gridded energy analyzer in electric propulsion applications. Note that for high voltage applications, the WAPA requires a high-voltage source meter to function since the anode is also the collector. In contrast, an RPA can have independent bias supply and current meter, which tends to be more readily available and much cheaper when compared to a high-voltage source meter.

Although the aligned-grid RPA was highly beneficial in targeted applications, the need for precise manufacturing and grid-to-grid alignment increased the overall production cost. The production cost of the aligned-grid RPA was about a factor of 2-3 times greater than that of the WAPA. A caveat was that there was not an easy way to compare the cost of the electronics associated with the RPA versus the WAPA as there was a single set of electronic circuitries driving both sensors. No direct cost comparison could be made with the unaligned-grid RPA since those were laboratory units.

6. Summary

The SEP PDP project completed engineering development of energy analyzers for NASA's Solar Electric Propulsion Plasma Diagnostics Package, and many plasma sensor related lessons were learned. In particular, designs for three types of aligned-grid RPA, one type of unaligned-grid RPA, and one type of WAPA were tested. Combined with detailed ion physics modeling, the development work showed that there were a variety of ways in which ions could impinge on the grids of the RPA if this sensor is not properly designed. To minimize anomalous features in the RPA traces, the aperture diameter of the electron suppression grid must be much larger than that of the bias grid. Furthermore, the team found that a type II RPA (bias aperture diameter smaller than repel aperture diameter) exhibited anomalous bias grid impingement, while a type III RPA (bias aperture diameter larger than repel aperture diameter) did not. In exchange, the effective retarding potential of the type III RPA was lower than the applied bias and was corrected using a simple scaling factor.

Comprehensive testing showed that aligned-grid RPAs had small acceptance angles ideal for focused applications while unaligned-grid RPAs and WAPAs had large acceptance angles and are better at measuring wide regions of the plume. The aligned-grid RPA and WAPA also had better transparencies than the unaligned-grid RPA, leading to better SNRs. Additionally, the aligned-grid RPA and WAPA had better energy resolution and were more compact than the unaligned-grid RPA.

The SEP PDP project greatly advanced flight plasma sensor design expertise and demonstrated the possibility of building highly capable potential analyzers tailored to demanding electric propulsion applications. The work of this project highlighted the value of ion trajectory simulations for designing RPAs and the potential of gridded energy analyzers for wider usage in electric propulsion.

7. References

[1] Lobbia, R. B., Singleton, J. T., Brown, D. L., Blakely, J. M., Reed, G. D., Bromaghim, D. R., Koo, J. W., Scharfe, M. K., Johnson, L. K., and Conroy, D., "Hall Thruster Plume Measurements: Aehf-2 on-Orbit Data, Ground Test Data, and Simulation Results", *60th Joint Army-Navy-NASA-Air Force Propulsion Meeting*, Colorado Springs, CO, Apr 29-May 2, 2013.

[2] Diamant, K. D., Liang, R., and Corey, R. L., "The Effect of Background Pressure on SPT-100 Hall Thruster Performance", *50th AIAA/ASME/SAE/ASEE Joint Propulsion Conference*, AIAA-2014-3710, Cleveland, OH, Jul 28-30, 2014. https://doi.org/10.2514/6.2014-3710

[3] Huang, W., Kamhawi, H., and Haag, T. W., "Effect of Background Pressure on the Performance and Plume of the HiVHAc Hall Thruster", *33rd International Electric Propulsion Conference*, 2013-058, Washington, DC, Oct 6-10, 2013.

[4] Frieman, J. D., "Characterization of Background Neutral Flows in Vacuum Test Facilities and Impacts on Hall Effect Thruster Operation", Ph.D. Dissertation, Aerospace Engineering, Georgia Institutde of Technology, Atlanta, GA, 2017.

[5] Brown, D. L., Lobbia, R. B., Hartley, K. D., Sekerak, M. J., King, D. Q., and Peterson, P. Y., "The Xr-5 and Xr-5a Hall Thrusters, Part 1: Stability and Mode Transitions", *62nd Joint Army-Navy-NASA-Air Force Propulsion Meeting*, Nashville, TN, Jun 1-4, 2015.

[6] Beal, B. E., Bromaghim, D. R., Spanjers, G., Fetrow, M., and Bemish, R., "Performance Characterization of a Modified Hall Thruster Onboard the X-37b Space Vehicle", *Joint Army-Navy-NASA-Air Force: 8th Spacecraft Propulsion Joint Subcommittee Meeting*, Phoenix, AZ, Dec 5-8, 2016.

[7] Manzella, D. H., Jankovsky, R. S., Elliott, F., Mikellides, I. G., Jongeward, G., and Allen, D., "Hall Thruster Plume Measurements on-Board the Russian Express Satellites", *27th International Electric Propulsion Conference*, 2001-044, Pasadena, CA, Oct 15-19, 2001.

[8] Tajmar, M., Meissl, W., Gonzalez del Amo, J., Foing, B., Laakso, H., Noci, G., Capacci, M., Malkki, A., Schmidt, W., and Darnon, F., "Two Ways to Evaluate the Xe^+ Ion Flow Velocity in a Hall Effect Thruster", *40th AIAA/ASME/SAE/ASEE Joint Propulsion Conference*, AIAA-2004-3437, Fort Lauderdale, FL, Jul 11-14, 2004.
https://doi.org/10.2514/6.2004-3437

[9] Busek. *First Us Hall Thruster in Space, Tacsat-2*. 2006 [cited; Available from: http://busek.com/flightprograms__ts2.htm.

[10] Busek. *200w Hall Thruster System, Falconsat-5*. 2010 [cited; Available from: http://busek.com/flightprograms__fs5.htm.

[11] Johnson, L. K., de Soria-Santacruz Pich, M., Conroy, D., Lobbia, R. B., Huang, W., Choi, M., and Sekerak, M. J., "Flight Plasma Diagnostics for High-Power, Solar-Electric Deep-Space Spacecraft", *2018 IEEE Aerospace Conference*, 17877989, Big Sky, MT, Mar 3-10, 2018.
https://doi.org/10.1109/AERO.2018.8396825

[12] Brown, D. L., "Electric Propulsion Test & Evaluation Methodologies for Plasma in the Environments of Space and Testing (Ep Tempest) - Program Review", *National Technical Information Service*, ADA627202, 2015.

[13] Kinefuchi, K., Koga, K., Kusawake, H., Tsuchiya, Y., Kubota, K., Cho, S., Sano, T., Fukatsu, T., Terakado, Y., Hatta, S., and Yamamoto, N., "On-Board Plasma Plume Diagnostics for Ets-9 All-Electric Satellite", *36th International Electric Propulsion Conference*, 2019-449, Vienna, Austria, Sep 15-20, 2019.

[14] Trottenberg, T., Bansemer, F., Böttcher, S., Feili, D., Henkel, H., Hesse, M., Kersten, H., Krüger, T., Laube, J., Lazurenko, A., Sailer, D., Schuster, B., Seimetz, L., Spethmann, A., Weis, S., and Wimmer-Schweingruber, R. F., "An in-Flight Plasma Diagnostic Package for Spacecraft with Electric Propulsion", *EPJ Techniques and Instrumentation*, Vol. 8, Oct 27, 2021, pp. 16.
https://doi.org/10.1140/epjti/s40485-021-00073-8

[15] Huang, W., Ahern, D. M., and Yim, J. T., "Lessons Learned from Development of Solar Electric Propulsion Plasma Diagnostics Package Sensors", *JANNAF 12th Spacecraft Propulsion Subcommittee Meeting*, Huntsville, AL, Dec 5-9, 2022.

[16] Brophy, J. R., Katz, I., Polk, J. E., and Anderson, J. R., "Numerical Simulations of Ion Thruster Accelerator Grid Erosion", *38th AIAA/ASME/SAE/ASEE Joint Propulsion Conference & Exhibit*, AIAA-2002-4261, Indianapolis, IN, Jul 7-10, 2002.
https://doi.org/10.2514/6.2002-4261

[17] Adams, B. M., Bohnhoff, W. J., Dalbey, K. R., Ebeida, M. S., Eddy, J. P., Eldred, M. S., Hooper, R. W., Hough, P. D., Hu, K. T., Jakeman, J. D., Khalil, M., Maupin, K. A., Monschke, J. A., Ridgway, E. M., Rushdi, A. A., Seidl, T., Stephens, A., Swiler, L. P., and Winokur, J. G., "Dakota, a Multilevel Parallel Object-Oriented Framework for Design Optimization, Parameter Estimation, Uncertainty Quantification, and Sensitivity Analysis: Version 6.13 User's Manual", *Sandia Technical Report SAND2020-12495*, Nov, 2020.

[18] Huang, W., Shastry, R., Soulas, G. C., and Kamhawi, H., "Farfield Plume Measurement and Analysis on the NASA-300M and NASA-300ms", *33rd International Electric Propulsion Conference*, 2013-057, Washington, DC, Oct 6-10, 2013.

[19] Huang, W., Kamhawi, H., Haag, T. W., Lopez Ortega, A., and Mikellides, I. G., "Facility Effect Characterization Test of NASA's HERMeS Hall Thruster", *52nd AIAA/SAE/ASEE Joint Propulsion Conference*, AIAA-2016-4828, Salt Lake City, UT, Jul 25-27, 2016.
https://doi.org/10.2514/6.2016-4828

[20] Hall, S. J., Jorns, B. A., Gallimore, A. D., Kamhawi, H., and Huang, W., "Plasma Plume Characterization of a 100 kW Nested Hall Thruster", *Journal of Propulsion and Power*, Vol. 38, No. 1, Jul 30, 2021.
https://doi.org/10.2514/1.B38081

[21] Yim, J. T., Huang, W., and Allen, M. G., "Extraction of Thruster Plume Ion Population Trends from Retarding Potential Analyzer Data", *International Electric Propulsion Conference 2024*, 2024-116, Toulouse, France, Jun 23-28, 2024.

[22] Peterson, P. Y., Kamhawi, H., Huang, W., Yim, J. T., Herman, D. A., Williams, G. J., Gilland, J. H., and Hofer, R. R., "NASA's HERMeS Hall Thruster Electrical Configuration Characterization", *52nd AIAA/SAE/ASEE Joint Propulsion Conference*, AIAA-2016-5027, Salt Lake City, UT, Jul 25-27, 2016.
https://doi.org/10.2514/6.2016-5027

[23] Huang, W., Gilland, J. H., Herman, D. A., Zuo, L., Feng, C., Wright, P., Johnson, I., Mullins, C., and Hohman, K., "A Facility Effect Characterization Test of the BHT-6000 Hall Thruster", *2024 AIAA SciTech Forum*, AIAA-2024-2366, Orlando, FL, Jan 8-12, 2024.
https://doi.org/10.2514/6.2024-2366

[24] Hofer, R. R., Lobbia, R. B., Chaplin, V. H., Lopez Ortega, A., Mikellides, I. G., Polk, J. E., Kamhawi, H., Frieman, J. D., Huang, W., Peterson, P. Y., and Herman, D. A., "Completing the Development of the 12.5 kW Hall Effect Rocket with Magnetic Shielding (HERMeS)", *36th International Electric Propulsion Conference*, 2019-193, Vienna, Austria, Sep 15-20, 2019.

[25] Huang, W., Williams, G. J., Peterson, P. Y., Kamhawi, H., Gilland, J. H., and Herman, D. A., "Plasma Plume Characterization of the HERMeS During a 1722-Hr Wear Test Campaign", *35th International Electric Propulsion Conference*, 2017-307, Atlanta, GA, Oct 8-12, 2017.

[26] Frieman, J. D., Kamhawi, H., Mackey, J. A., Peterson, P. Y., Gilland, J. H., Hofer, R. R., Inaba, D., Dao, H., Branch, N. A., and Welander, B., "Extended Wear Testing of the 12-kW Advanced Electric Propulsion System Engineering Test Unit Hall Thruster", *International Electric Propulsion Conference 2022*, 2022-362, Boston, MA, Jun 19-23, 2022.

[27] Frieman, J. D., Kamhawi, H., Huang, W., Mackey, J. A., Ahern, D. M., Peterson, P. Y., Gilland, J. H., Hall, S. J., Hofer, R. R., Branch, N. A., Dao, H., Inaba, D., and Welander, B., "Performance of the 12.5-kW Advanced Electric Propulsion System Engineering Test Unit Hall Thruster", *68th Joint Army-Navy-NASA-Air Force Propulsion Meeting*, Virtual, Jun 7-17, 2021.

[28] Huang, W., Frieman, J. D., Kamhawi, H., Peterson, P. Y., and Hofer, R. R., "Ion Velocity Characterization of the 12.5-kW Advanced Electric Propulsion System Engineering Hall Thruster", *2021 AIAA Propulsion and Energy Forum*, AIAA-2021-3432, Virtual, Aug 9-11, 2021.
https://doi.org/10.2514/6.2021-3432

[29] Savitzky, A. and Golay, M. J. E., "Smoothing and Differentiation of Data by Simplified Least Squares Procedures", *Analytical Chemistry*, Vol. 36, No. 8, Jul, 1964, pp. 1627-1639.
https://doi.org/10.1021/ac60214a047

[30] Steinier, J., Termonia, Y., and Deltour, J., "Comments on Smoothing and Differentiation of Data by Simplified Least Squares Procedure", *Analytical Chemistry*, Vol. 44, No. 11, Sep, 1972, pp. 1906-1909.
https://doi.org/10.1021/ac60319a045

[31] Hutchinson, I. H., *Principles of Plasma Diagnostics*, 2nd ed., Cambridge University Press, 2002.
https://doi.org/10.1017/CBO9780511613630